

Z ~ 1 LY α EMITTERS I. THE LUMINOSITY FUNCTION^{1, 2, 3, 4}

ISAK G. B. WOLD⁵, AMY J. BARGER^{5,6,7}, AND LENNOX L. COWIE⁷

Draft version May 2, 2018

ABSTRACT

We construct a flux-limited sample of 135 candidate $z \sim 1$ Ly α emitters (LAEs) from *Galaxy Evolution Explorer* (*GALEX*) grism data using a new data cube search method. These LAEs have luminosities comparable to those at high redshifts and lie within a 7 Gyr gap present in existing LAE samples. We use archival and newly obtained optical spectra to verify the UV redshifts of these LAEs. We use the combination of the *GALEX* UV spectra, optical spectra, and X-ray imaging data to estimate the active galactic nucleus (AGN) fraction and its dependence on Ly α luminosity. We remove the AGNs and compute the luminosity function (LF) from 60 $z \sim 1$ LAE galaxies. We find that the best fit LF implies a luminosity density increase by a factor of ~ 1.5 from $z \sim 0.3$ to $z \sim 1$ and ~ 20 from $z \sim 1$ to $z \sim 2$. We find a $z \sim 1$ volumetric Ly α escape fraction of $0.7 \pm 0.4\%$.

Subject headings: cosmology; observations

1. INTRODUCTION

Ly α emitters (LAEs) have the potential to be a powerful cosmological probe. The evolution of their number density at $z \gtrsim 7$ offers the opportunity to constrain the opacity of the intergalactic medium (IGM) and the timing of cosmic reionization (e.g., Stark et al. 2011). Their clustering properties may be able to constrain efficiently the expansion history of the universe (e.g., Hill et al. 2008; Greig et al. 2013). Furthermore, at the highest redshifts ($z > 6$) Ly α is the only emission line that we can detect from the ground, making it the only probe of the internal structure of these galaxies. However, to use LAEs as probes of the high-redshift universe, we must first understand their physical properties.

The Ly α line is resonantly scattered by neutral hydrogen, making its flux and line profile notoriously hard to interpret (e.g., Neufeld 1991; Kunth et al. 2003; Finkelstein et al. 2007; Schaerer & Verhamme 2008; Östlin et al. 2009). For example, unlike rest-frame UV continuum observations, one cannot merely apply a dust extinction correction to obtain an estimate of the star formation rate (SFR). Thus, constraints on the Ly α escape fraction must be empirically measured. Furthermore, ob-

servational studies are required to determine which physical properties facilitate the escape of Ly α emission.

Due to the limited resources in the UV, most observational studies have focused on constraining the physical properties of $z \sim 2 - 3$ LAEs, where the Ly α line moves into the optical. Detailed analysis of the host galaxies is difficult at these high redshifts, and different groups have come to drastically different conclusions about them (e.g., compare Hu et al. 1998; Nilsson et al. 2007; Gawiser et al. 2007 to Lai et al. 2008; Kornei et al. 2010). Furthermore, at these redshifts Ly α emission may be significantly altered by the intervening IGM. For example, based on hydro-simulations, Laursen et al. (2011) find that only $\sim 70\%$, 26% , and 20% of Ly α photons are transmitted through the IGM at $z \sim 3.5$, 5.8 , and 6.5 , respectively. To make progress, we need to study lower-redshift samples where LAEs are bright due to smaller luminosity distances and where LAEs can be integrated into comprehensive studies of galaxies at the same redshifts to understand how LAEs are drawn from the general galaxy population.

Recently, a $z \sim 0.3$ LAE sample has been found by searching for emission-line objects in *Galaxy Evolution Explorer* (*GALEX*; Martin et al. 2005) FUV pipeline spectra. Since the *GALEX* grism pipeline only includes objects whose UV continuum magnitudes are bright enough to generate measurable continuum spectra, only a fraction of the emission-line objects are extracted. Thus, this sample's selection process is most analogous to locating LAEs in the high-redshift Lyman break galaxy (LBG) population via spectroscopy (e.g., Shapley et al. 2003). However, the procedure enables the selection of a substantial sample of $z \sim 0.3$ sources, and many papers have investigated their properties (e.g., Deharveng et al. 2008; Finkelstein et al. 2009; Atek et al. 2009; Scarlata et al. 2009; Cowie et al. 2010, 2011). The picture that emerged from the optical follow-up of the $z \sim 0.3$ *GALEX* sample is that LAEs, when compared to UV-continuum selected galaxies, are relatively young, compact, metal poor, star-forming galaxies (Cowie et al. 2010, 2011).

However, it is not clear that the properties of these

¹ Based in part on data obtained from the Mikulski Archive for Space Telescopes (MAST). STScI is operated by the Association of Universities for Research in Astronomy, Inc., under NASA contract NAS5-26555. Support for MAST for non-HST data is provided by the NASA Office of Space Science via grant NNX09AF08G and by other grants and contracts.

² The W. M. Keck Observatory is operated as a scientific partnership among the the California Institute of Technology, the University of California, and NASA, and was made possible by the generous financial support of the W. M. Keck Foundation.

³ Some of the observations reported in this paper were obtained with the Southern African Large Telescope (SALT).

⁴ Based in part on zCOSMOS observations carried out using the Very Large Telescope at the ESO Paranal Observatory under Programme ID: LP175.A-0839.

⁵ Department of Astronomy, University of Wisconsin-Madison, 475 North Charter Street, Madison, WI 53706, USA; wold@astro.wisc.edu, barger@astro.wisc.edu

⁶ Department of Physics and Astronomy, University of Hawaii, 2505 Correa Road, Honolulu, HI 96822, USA

⁷ Institute for Astronomy, University of Hawaii, 2680 Woodlawn Drive, Honolulu, HI 96822, USA

low-redshift ($z \sim 0.3$) sources are representative of high-redshift LAEs. In particular, LAEs are considerably fainter and much less common at $z \sim 0.3$ than they were in the past, with only about 5% of $z \sim 0.3$ UV-continuum selected galaxies having rest-frame Ly α equivalent widths ($EW_r(\text{Ly}\alpha)$) greater than 20 Å, compared with 20% – 25% at $z \sim 3$ (Shapley et al. 2003). The $EW_r(\text{Ly}\alpha) \geq 20\text{Å}$ requirement is typically used to define high-redshift samples (e.g., Hu et al. 1998). The first redshift where LAEs are seen that are comparable in luminosity to high-redshift LAEs is at $z \sim 1$. However, only a handful of $z \sim 1$ LAEs have *GALEX* detectable continuum spectra. Thus, we need to remove the pipeline’s continuum selection requirement ($\text{NUV} < 22$) in order to study a large sample of $z \sim 1$ LAEs. This has the additional virtue of producing a purely flux-limited sample that is straightforward to analyze.

In Barger, Cowie, & Wold (2012, hereafter, BCW12), we solved the problem of obtaining a flux-limited sample of $z \sim 1$ LAEs for the *Chandra* Deep Field-South (CDFs). To do this, we converted the multiple *GALEX* grism images into a three-dimensional (two spatial axes and one wavelength axis) data cube. We then treated the wavelength “slices” as narrowband images in which we searched for emission-line galaxies. Through simulations, we showed that we could recover more than 80% of the sources with $f(\text{Ly}\alpha) \gtrsim 10^{-15} \text{ erg cm}^{-2} \text{ s}^{-1}$, which corresponds to $L(\text{Ly}\alpha) \gtrsim 10^{42.5} \text{ erg s}^{-1}$ at $z \sim 1$. By comparing our sample to X-ray data, existing optical spectroscopy, and deep *U*-band imaging, we determined that nearly all of our 28 new LAEs are real and that the UV spectroscopic redshifts based on the Ly α identifications are reliable. We also determined the fraction of active galactic nuclei (AGNs) in the sample relative to star formers.

In this paper, we apply the data cube search method to all of the deepest *GALEX* grism fields (CDFs-00, 353 ks; GROTH-00, 291 ks; NGPDWS-00, 165 ks; COSMOS-00, 140 ks), which correspond to some of the most intensively studied regions in the sky. This work provides the first large sample of $z = 0.67 - 1.16$ LAEs ($N=60$) that can be used to investigate the physical properties of these galaxies. There are relatively large samples of known LAEs at redshifts of $z \sim 0.3$ and $z \sim 2$. Thus, a sample of $z \sim 1$ LAEs is needed to map the evolution of LAEs over a ~ 7 Gyr gap. This redshift regime is where the star-forming properties of galaxies change very rapidly and where the star formation begins to decline. It is a key area for connecting to the high-redshift universe.

In Paper II, we will leverage existing archival spectra and followup optical spectra to constrain their physical properties. In particular, we will study which properties facilitate the escape of Ly α emission and how LAEs are drawn from the overall galaxy population. This will help us understand how the Ly α emission properties of galaxies evolve as we move to higher redshifts and higher Ly α luminosities.

Here we catalog our candidate $z \sim 1$ LAE samples in each field and give optical redshifts from both archival and newly obtained observations. With X-ray, UV, and optical data, we determine the false detection rate (cases where the emission line is either not confirmed or is not Ly α) and the AGN contamination rate of our sample.

With the remaining LAEs, we compute the LAE galaxy luminosity function (LF) at $z \sim 1$ and use this to investigate the evolution of the Ly α LF and the Ly α escape fraction over the redshift range from $z \sim 0.3$ to $z \sim 2$. Unless otherwise noted, we give all magnitudes in the AB magnitude system ($m_{\text{AB}} = 23.9 - 2.5 \log_{10} f_\nu$ with f_ν in units of μJy). We use a standard $H_0 = 70 \text{ km s}^{-1} \text{ Mpc}^{-1}$, $\Omega_M = 0.3$, and $\Omega_\Lambda = 0.7$ cosmology.

2. CHOICE OF FIELDS

We study the four deepest NUV grism observations: CDFS-00, GROTH-00, NGPDWS-00, and COSMOS-00. The *GALEX* fields are large ($\sim 1 \text{ deg}^2$), but in subregions of the fields, there are many objects with optical spectra (CDFs, Vanzella et al. 2008, Popesso et al. 2009; GROTH, Newman et al. 2012; COSMOS, Lilly et al. 2007, Trump et al. 2009). In subregions, there are also multi-color observations from the *HST* GOODS (Giavalisco et al. 2004), CANDELS (Grogin et al. 2011; Koekemoer et al. 2011), COSMOS (Leauthaud et al. 2007), and GEMS (Rix et al. 2004) programs that provide the galaxy morphologies and spectral energy distributions from the rest-frame far-UV to the mid-infrared. When corrected for the emission-line contributions using the spectra (Schaerer & de Barros 2009; Atek et al. 2011; Cowie et al. 2011), the spectral energy densities can be used to compute the ages and extinctions of the galaxies.

Finally, the 4 Ms *Chandra* image of the CDFS (Alexander et al. 2003; Luo et al. 2008) region, along with shallower X-ray observations in the Extended CDFS (Lehmer et al. 2005; Virani et al. 2006), COSMOS (Elvis et al. 2009), GROTH (Laird et al. 2009), and NGPDWS (Kenter et al. 2005) fields, can be used to identify AGNs. AGNs may also be identified using the UV grism spectra obtained with *GALEX* and the optical spectra, but the X-rays provide a valuable cross-check, where they are available.

3. *GALEX* NUV LAES

3.1. Catalog Extraction

As described in BCW12, we converted multiple *GALEX* NUV grism images into a three-dimensional (two spatial axes and one wavelength axis) data cube. Each background subtracted data cube consists of thirty 20 Å narrowband slices covering a wavelength range of 2030 to 2630 Å and a $50' \times 50'$ field of view. We used SExtractor (Bertin & Arnouts 1996) to identify all 4σ sources within the cube and then visually inspected each source and its spectrum (1-D and 2-D) to eliminate objects that were artifacts. Applying the data cube search produced 40 CDFS, 41 GROTH, 35 NGPDWS, and 19 COSMOS objects for a full Ly α selected candidate sample of 135 (see Table 1). In Figure 1(a), we show the extracted 1-D spectrum for GALEX033100-273020 to illustrate the quality of our *GALEX* spectra. BCW12 performed this routine on the deepest NUV grism field (CDFs-00). To verify the BCW12 sample of 28 LAE candidates, we have independently searched the CDFS cube for emission-line sources. We found 27 of the 28 objects that were identified by BCW12, and we found 12 new objects. Approximately half of these new LAE candidates are close to the field’s 80% completeness flux threshold (see Section 3.3) and

Table 1

GALEX field exposure time, 80% completeness flux threshold, number of LAE candidates, and number of confirmed LAE galaxies

<i>GALEX</i> Field (1)	α (J2000.0) (2)	δ (J2000.0) (3)	Exp. time (4)	$f_{\text{Ly}\alpha}$ (erg cm $^{-2}$ s $^{-1}$) (5)	Num. LAE candidates (6)	Num. confirmed LAEs (7)
CDFS	3 ^h 30 ^m 40 ^s	-27° 27' 43"	353 ks	1.8×10^{-15}	40	24
GROTH	14 ^h 19 ^m 58 ^s	52° 46' 54"	291 ks	2.0×10^{-15}	41	19
NGPDWS	14 ^h 36 ^m 37 ^s	35° 10' 17"	165 ks	2.3×10^{-15}	35	11
COSMOS	10 ^h 00 ^m 29 ^s	+2° 12' 21"	140 ks	3.2×10^{-15}	19	4

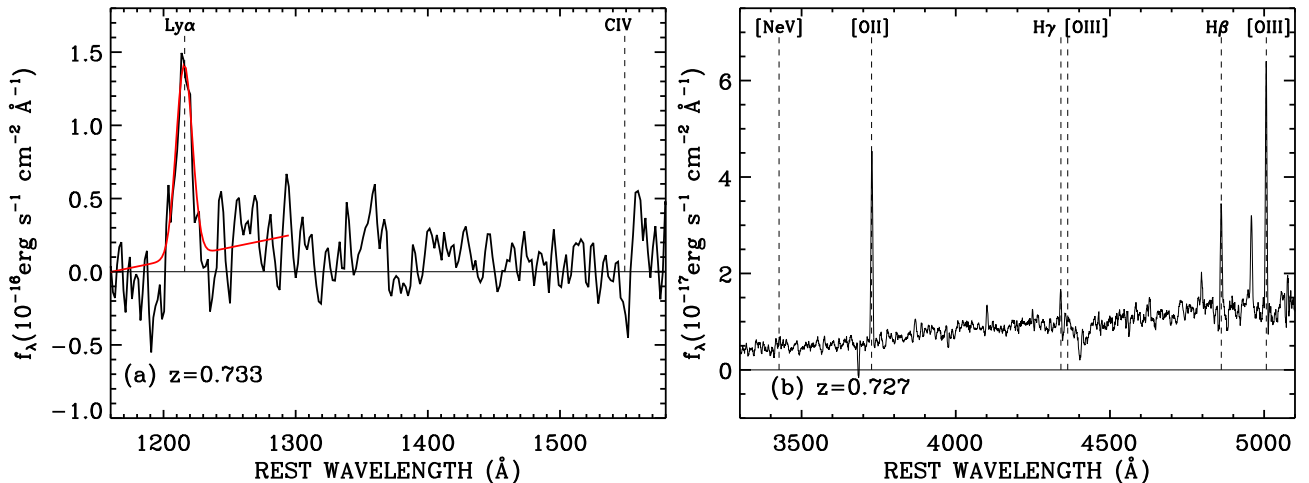


Figure 1. (a) LAE galaxy UV spectrum GALEX033100-273020. The redshift ($z = 0.733$) and Ly α flux is measured from the Gaussian fit (red profile). The lack of detected CIV λ 1549 is consistent with this source being star-forming galaxy rather than AGN. (b) Keck-DEIMOS spectrum for the same source. The optical redshift ($z = 0.727$) is found to be consistent with the UV redshift. The lack of detected [NeV] λ 3426 or broad Balmer lines is consistent with this source being star-forming galaxy rather than AGN.

(A color version of this figure is available in the online journal.)

were probably missed due to their faintness. The other half are relatively bright and were probably mis-classified as data cube artifacts, such as the remaining edge effects from brighter objects. The BCW12 LAE candidate missed by this search (GALEX033124-275625) is real and has a consistent optical redshift. This LAE was eliminated in the visual inspection phase of our search due to its proximity to a UV-bright star. We include this missed LAE in all subsequent analysis. To date, we have confirmed the UV redshifts of 92% (11 out of 12) of the newly discovered CDFS LAEs with optical follow-up spectra.

3.2. Optical Spectroscopic Followup

Spectroscopic observations were primarily obtained with the DEep Imaging Multi-Object Spectrograph (DEIMOS; Faber et al. 2003) on Keck II in a series of runs in 2012 to 2013. The observations were made with the ZD600 line mm $^{-1}$ grating blazed at 7500 Å. This gives a resolution of ~ 5 Å with a 1" slit and a wavelength coverage of 5300 Å. The high spectral resolution is necessary to distinguish the [OII] λ 3727 doublet structure. The observations were not generally taken at parallactic angle, since the position angle was determined by the mask orientation. Each ~ 30 min exposure was broken into three subsets, with the objects stepped along the slit by 1.5" in each direction. The raw two-dimensional spectra were reduced and extracted using the procedure described in Cowie et al. (1996). In Figure 1(b), we show the optical spectrum for GALEX033100-273020 to illus-

trate the quality of our DEIMOS spectra. We used the remaining space available in our MOS masks to observe a control sample, a UV-continuum selected sample without detected Ly α that have the same luminosities and are expected, based on their colors, to lie in the same redshift interval as our primary LAE sample. In Paper II, we will use the control sample to determine how the LAE galaxies are drawn from the general galaxy population.

We observed our southern and equatorial fields (COSMOS and CDFS) with the Robert Stobie Spectrograph (RSS; Burgh et al. 2003) on SALT from 2011 to 2013. The observations were made with the pg1300 grating with the grating angle adjusted to ensure spectral coverage of lines redward of [NeV]. This gives a resolution of ~ 4 Å with a 1.5" slit and a wavelength coverage of 2000 Å. We observed each target for ~ 30 min. The raw two-dimensional spectra were reduced and extracted using the IRAF packages LONGSLIT and APEXTRACT.

3.3. Catalog Completeness

To determine the limitations of our multi-field catalogs and to compute the LAE galaxy LF, we have developed a simulation to determine the completeness of recovery versus flux. For each field, we added 1000 simulated emitters uniformly within the field's data cube. We did not model morphology or size difference, since nearly all emitters are unresolved at the spatial ($\sim 6''$) and spectral resolution (~ 25 Å) of the *GALEX* grism data.

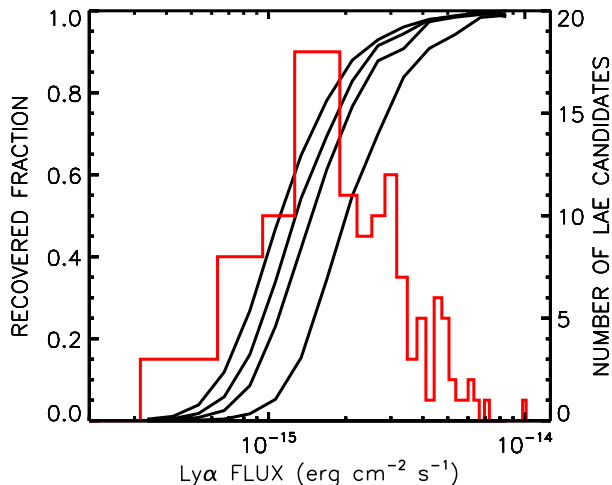


Figure 2. Fraction of simulated sources recovered as a function of the emission-line flux. From left to right the black curves show recovered fractions from CDFS, GROTH, NGPDWS, and COSMOS fields (also see Table 1). The red histogram shows the number of LAE candidates as a function of flux for all four *GALEX* fields. (A color version of this figure is available in the online journal.)

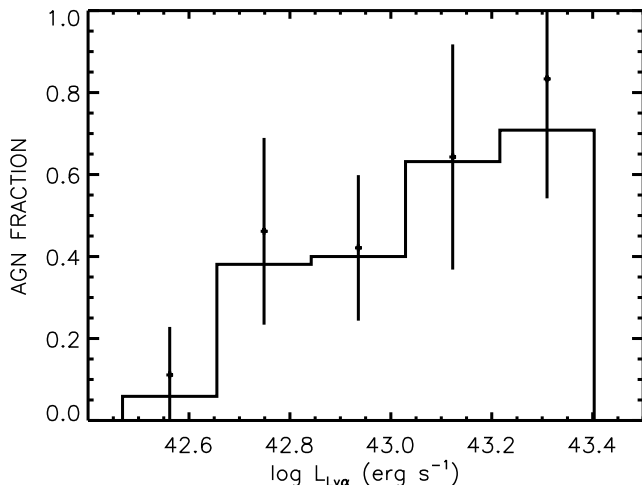


Figure 3. AGN fraction per $\text{Ly}\alpha$ luminosity bin for the $\text{EW}_r(\text{Ly}\alpha) \geq 20 \text{ \AA}$ LAE data cube sample. The histogram shows the sample wide AGN fractions, while the points with error bars show the AGN fractions for regions with deep X-ray data.

We then ran our standard selection procedure and found the number of recovered objects. We independently performed the above procedure ten times, giving a total of 10,000 input sources. In Table 1, we list the flux threshold above which each field is greater than 80% complete. As expected, the completeness limit scales as the inverse square root of the exposure time. Below this threshold, the completeness of our sample rapidly declines (see Figure 2).

3.4. Catalogs of LAE Candidates by Field

In Tables 4-7, we list all of the LAE candidates in the CDFS, GROTH, NGPDWS, and COSMOS fields ordered by redshift. In Column 1, we give the *GALEX* name; in Columns 2 and 3, the J2000 right ascension and declination based on NUV position; in Columns 4 and 5, the NUV and FUV AB magnitudes; in Column 6, the redshift from the *GALEX* UV spectrum; in Column 7, the logarithm of the $\text{Ly}\alpha$ luminosity; in Column 8,

the rest-frame $\text{EW}_r(\text{Ly}\alpha)$ with 1σ errors; in Column 9, the logarithm of the X-ray flux; in Column 10, the UV classified AGNs; in Columns 11 and 12, the J2000 right ascension and declination based on optical position; in Column 13, the offset between the optical to UV positions; in Column 14, the optical redshift; and in Column 15 the optically classified AGNs.

We measured NUV and FUV AB magnitudes from the archival *GALEX* background subtracted intensity maps (Morrissey et al. 2007). We first determined the magnitudes within $8''$ diameter apertures centered on each of the emitter positions. To correct for flux that falls outside our apertures, we measured the offset between $8''$ aperture magnitudes and *GALEX* pipeline total magnitudes for all bright cataloged objects (20-23 mag range) within our fields. We determined the median offset for each field and applied these to the magnitudes listed in Columns 4 and 5. All objects are bright in the NUV when compared to their FUV magnitudes. In some cases, we measure negative FUV fluxes. For these cases, we list the magnitude corresponding to the absolute value of the flux with a minus sign in front to indicate that the flux was negative.

We corrected our one-dimensional NUV spectra for Galactic extinction assuming a Fitzpatrick (1999) reddening law with $R_V=3.1$. We obtained A_V values from the Schlafly & Finkbeiner (2011) recalibration of the Cardelli et al. (1989) extinction map as listed in the NASA/IPAC Extragalactic Database (NED). Galactic extinction modifies the $\text{Ly}\alpha$ flux by $\sim 11\%$ for the COSMOS LAEs, $\sim 4\%$ for the GROTH LAEs, and $\sim 6\%$ for the CDFS and NGPDWS LAEs.

From these extinction corrected spectra, we measured the redshifts, the $\text{Ly}\alpha$ fluxes, and the line widths using a two step process. First, we fit a 140 \AA rest-frame region around the $\text{Ly}\alpha$ line with a Gaussian and a sloped continuum (see Figure 1(a)). A downhill simplex optimization routine was used to χ^2 fit the five free parameters (continuum level and slope plus Gaussian center, width, and area). We used the results of this fitting process to eliminate the two continuum parameters and as a starting point for the second step. In the second step, we used the IDL MPFIT procedures of Markwardt (2009) to χ^2 fit the remaining three Gaussian parameters. We also employed the same fitting routine but with only a flat continuum (one continuum free parameter instead of two). We find that our results are not significantly affected by this model assumption. With the best-fit redshifts and $\text{Ly}\alpha$ fluxes, we calculated $\text{Ly}\alpha$ luminosities. When available, we used the more precise optical redshift rather than the UV redshift to calculate the $\text{Ly}\alpha$ luminosities. We list the UV redshifts and $\text{Ly}\alpha$ luminosities in Columns 6 and 7.

The rest-frame $\text{EW}_r(\text{Ly}\alpha)$ measured on the spectra are quite uncertain due to the very faint UV continuum. We obtained a more accurate rest-frame EW by dividing the measured $\text{Ly}\alpha$ flux by the continuum flux measured from the broadband NUV image. It is these rest-frame EWs that are given in Column 8. In Section 5, we investigate the $z \sim 1$ rest-frame EW distribution.

We made a classification of whether the emitter was an AGN based on the presence of either broad or high-excitation emission lines in its UV or optical spectra or

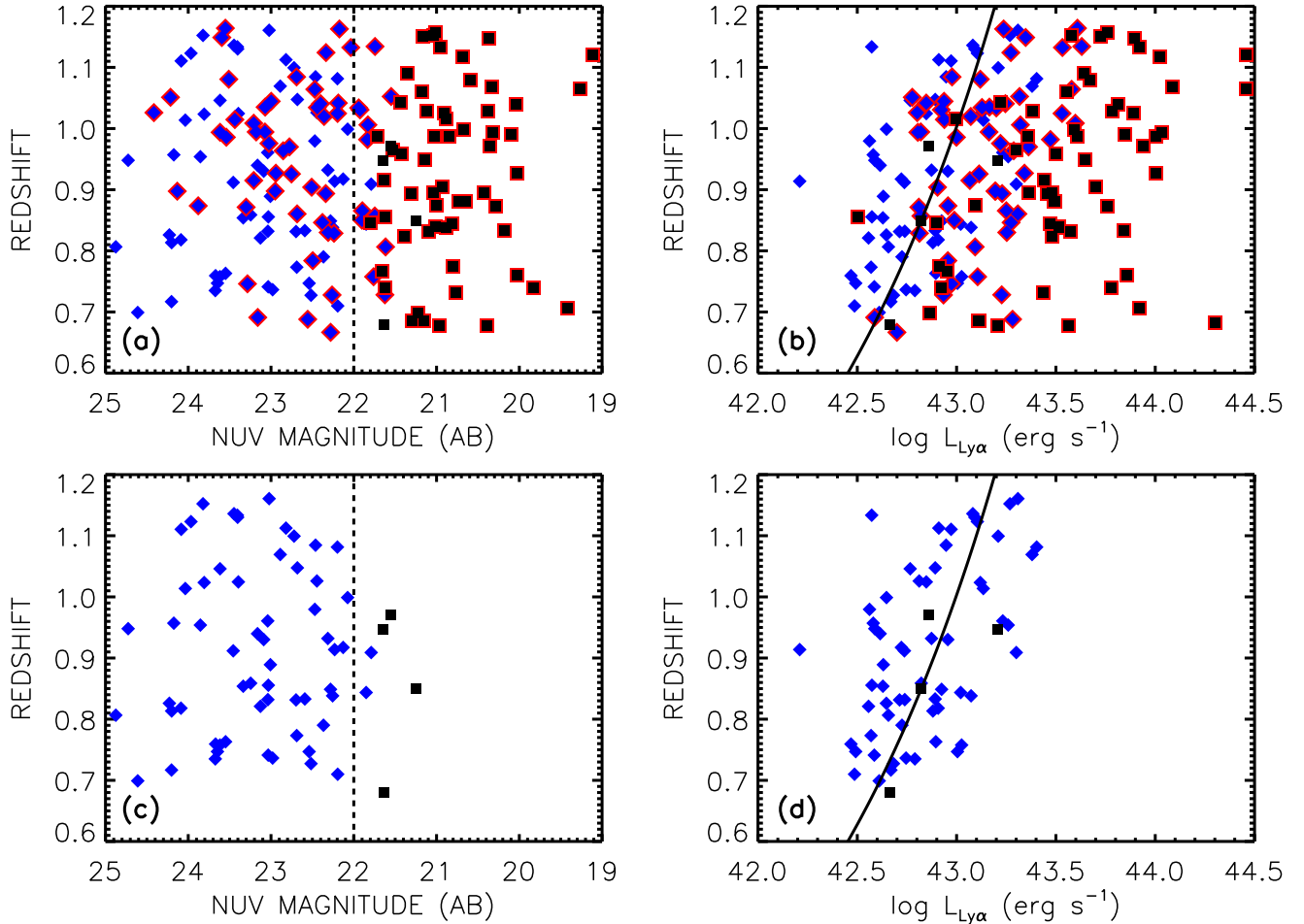


Figure 4. (a) LAE redshift vs. $\text{Ly}\alpha$ luminosity. Black squares show the pipeline LAEs found by Cowie et al. (2010, 2011) constrained to the data cubes’ $50' \times 50'$ FOVs and redshift range ($z = 0.67 - 1.16$). Blue diamonds show our data cube LAEs. Objects classified as AGNs in any way are surrounded by red. The dashed line shows the *GALEX* pipeline’s magnitude limit $\text{NUV} \sim 22$. (b) LAE redshift vs. $\text{Ly}\alpha$ luminosity. The solid line indicates the data cube’s $\sim 80\%$ flux completeness limit. (c) The same as Figure 4(a), but with all AGNs removed. (d) The same as Figure 4(b), but with all AGNs removed.

(A color version of this figure is available in the online journal.)

on the presence of an X-ray counterpart. Candidate X-ray counterparts were identified by matching all X-ray sources within a $6''$ radius from the data cube position. We then manually inspected the matches to reject false counterparts. We list the X-ray flux of each identified counterpart in Column 9. The X-ray luminosity threshold of $10^{42} \text{ erg s}^{-1}$ that is usually used to define AGN activity (Hornschemeier et al. 2001; Barger et al. 2002; Szokoly et al. 2004) corresponds to an X-ray flux of $\gtrsim 10^{-15.3} \text{ erg cm}^{-2} \text{ s}^{-1}$ for our $z > 0.67$ sample. All X-ray detected sources exceed this luminosity threshold, and we hereafter consider these sources to be AGNs. In Column 10, we list sources classified as AGNs based on the presence of broad or high-excitation emission lines in their UV spectrum (see, e.g., Cowie et al. 2010). Our candidate star-forming galaxy sample will still contain some remaining AGNs, so we used the optical spectra to make a final determination of whether a galaxy is, in fact, star-forming. In Column 15, we identify optical AGNs based on the presence of either detectable [NeV] or broad Balmer or $\text{MgII}\lambda 2798$ emission lines in the optical spectra.

We obtained optical redshifts for 122 of our 135 can-

didate LAEs. We found that 15 optical redshifts did not match the measured UV redshifts. For these objects, the $\text{Ly}\alpha$ luminosity and the rest-frame $\text{EW}_r(\text{Ly}\alpha)$ fields are left blank in Columns 7 and 8. These sources are either spurious, stars, or strong $\text{CIV}\lambda 1549$ emitters. For example, we found three LAE candidates in our COSMOS-00 field to be $z \sim 0.35$ $\text{CIV}\lambda 1549$ emitters. We indicate these objects by showing their optical redshift in parentheses or by setting their optical redshift and type to ‘star’ in Columns 14 and 15. Additionally, we observed 4 candidate LAEs with Keck DEIMOS without recovering an optical redshift. We indicate these objects by setting their optical redshifts to ‘no z’ in Column 14. For the purpose of computing the LF, we retain the NUV brightest ‘no z’ source (GALEX033045-274506), which has two nearby untargeted potential optical counterparts. The remaining ‘no z’ candidate LAEs have relatively faint NUV counterparts and may be spurious. Given the spatial resolution of our data cubes ($\sim 6''$), we find that a total of five ‘no z’ and non-matching redshift sources have potential alternative optical counterparts. We list these [alt] sources in the Table 4-7 notes. Overall, we exclude 18 optically unconfirmed LAE candidates in the

following discussion and in the construction of the $z \sim 1$ Ly α LF.

Excluding these 18, we are left with a sample of 117 LAEs. We classified 57 of these sources as UV, X-ray, or optical AGN. This establishes an AGN fraction (f_{AGN}) of $49\% \pm 8\%$ for our sample. After we exclude UV identified AGNs, our f_{AGN} drops to $41\% \pm 8\%$. When performing the optical spectroscopic followup, we preferentially targeted LAEs that were not classified as UV or X-ray AGNs. With this policy, we obtained optical redshifts for 98% (59 out of 60) of our LAE galaxies but only 89% (51 out of 57) of our AGNs. We found that 9 of the 37 LAEs classified as X-ray AGNs were already classified as AGNs based on their UV spectra. We observed 19 LAEs classified as X-ray AGNs with Keck DEIMOS. Only 3 of these X-ray AGNs were not classified as optical AGNs.

As a cross check to our sample's AGN fraction of $49\% \pm 8\%$, we only consider LAEs within deep X-ray fields and re-compute the AGN fraction. There are 79 candidate LAEs within deep X-ray fields; we classified 44 (or $56\% \pm 10\%$) as AGNs. This is not significantly different our sample-wide AGN contamination. In Figure 3, we show that the AGN fraction increases with Ly α luminosity (similar trends have been noted by Cowie et al. 2010 and Nilsson & Møller 2011). Breaking each sample into 5 luminosity bins from $\log L_{\text{Ly}\alpha} = 42.5$ to 43.4 (used below in the Ly α LF computation) and requiring $\text{EW}_r(\text{Ly}\alpha) \geq 20 \text{ \AA}$, we find that the AGN fraction increases from 6% to 71% for the full *GALEX* data cube sample and from 13% to 83% for the deep X-ray subsample. Given this small but systematic difference, we derive the Ly α LF for our full LAE galaxy sample and for the subsample limited to regions with deep X-ray data to determine the effect, if any, on our results.

In common with other low-redshift samples, our AGN fraction is high compared to the AGN fractions quoted for higher redshift samples. (Note that many of the low-redshift samples quote AGN fractions that exclude sources known to be AGNs based on the UV spectra; our AGN fraction includes these sources.) However, it is essential to emphasize that the AGN fraction is strongly dependent on the luminosity range. Our LAEs have Ly α luminosities from $10^{42.2}$ to $10^{43.6} \text{ erg s}^{-1}$. As shown in Nilsson & Møller (2011), the AGN fraction rapidly increases over this range and approaches 100% at Ly α luminosities above $10^{43.6} \text{ erg s}^{-1}$.

The high-luminosity LAEs are primarily AGNs, and it is these objects that are included in the *GALEX* pipeline extractions. Only with the increased sensitivity of the data cube search do we probe faint enough to develop large samples of star-forming LAEs. In Figure 4(a), we show the LAE redshift versus the NUV magnitudes for our LAE data cube sample (blue diamonds) and for the pipeline LAE sample found by Cowie et al. (2010, 2011, black squares) constrained to the data cubes' $50' \times 50'$ FOVs and redshift range ($z = 0.67 - 1.16$). We note that there are seven pipeline LAE galaxies listed within the CDFS, GROTH, NGPDWS, and COSMOS fields (see Table 2 in Cowie et al. 2011). We excluded one pipeline LAE galaxy due to its low redshift $z = 0.65$, and we excluded two pipeline LAE galaxies because they do not fall within our data cubes' $50' \times 50'$ FOVs. Although not excluded for the purposes of this discussion, if we also

Table 2
Luminosity function minimum Ly α flux and corresponding completeness limit

<i>GALEX</i> Field (1)	$f_{\text{Ly}\alpha}$ (erg cm $^{-2}$ s $^{-1}$) (2)	Completeness (3)
CDFS	8.5×10^{-16}	26.4%
GROTH	5.2×10^{-16}	1.6%
NGPDWS	10.9×10^{-16}	24.6%
COSMOS	24.1×10^{-16}	62.3%

require $\text{EW}_r(\text{Ly}\alpha) \geq 20 \text{ \AA}$, then there are only two LAE galaxies that remain in the pipeline sample. By construction, the *GALEX* pipeline extractions miss all LAEs fainter than the pipeline magnitude limit of $\text{NUV} \sim 22$ (dashed line in Figure 4(a)). Objects classified as AGNs in any way have their symbols outlined in red. In Figure 4(b), we show the LAE redshift versus the Ly α luminosity. Directly below Figures 4(a) and 4(b), we show these Figures again but with all AGNs removed. We find that the AGN fraction reaches 100% at a Ly α luminosity of $\sim 10^{43.5} \text{ erg s}^{-1}$. This is also the Ly α luminosity where the pipeline extraction begins to miss sources. While there is some luminosity overlap between the data cube and pipeline samples, we find that our data cube search is necessary to obtain a large LAE galaxy sample.

4. LUMINOSITY FUNCTION

We computed the Ly α LF of the combined CDFS, GROTH, NGPDWS, and COSMOS LAE galaxy samples in the redshift range $z = 0.67 - 1.16$ using the 1/V technique (Felten 1976). We only included sources that were not classified as AGN in any way and that have $\text{EW}_r(\text{Ly}\alpha) \geq 20 \text{ \AA}$. With these criteria, the sample includes two LAE galaxies, which appeared in the pipeline sample of Cowie et al. (2011, see their Table 2). The rest (58) come from our data cube sample and are not found in the *GALEX* pipeline extractions.

To compute the LF, we divided our Ly α survey into 20 samples (5 samples per field), where the sample j covers a Ly α flux range $f_{1j} \leq f \leq f_{2j}$ and a solid angle area ω_j (the masking of bright sources alters ω_j from one *GALEX* $50' \times 50'$ field to another). For each field, we took the difference between the minimum and maximum observed Ly α flux and divided this into 5 flux bins of equal size (see Table 2 for minimum Ly α flux values and corresponding completeness limits). The sampling rate S_j (the fraction of LAE galaxies in the given flux range that were observed) was estimated with our completeness simulations. The effective area of a sample is $\Omega_j = \omega_j S_j$. The accessible volume of the i^{th} LAE galaxy in sample j is

$$V_{ij} = \Omega_j \left(V(z_{max}^{ij}) - V(z_{min}^{ij}) \right),$$

where the comoving volume is calculated at the highest and lowest redshifts at which the i^{th} LAE galaxy remains both within sample j 's Ly α flux range $f_{1j} \leq f \leq f_{2j}$ and within the redshift range $z = 0.67 - 1.16$. The total accessible volume of the i^{th} LAE galaxy is

$$V_i = \sum_{j=1}^{20} V_{ij},$$

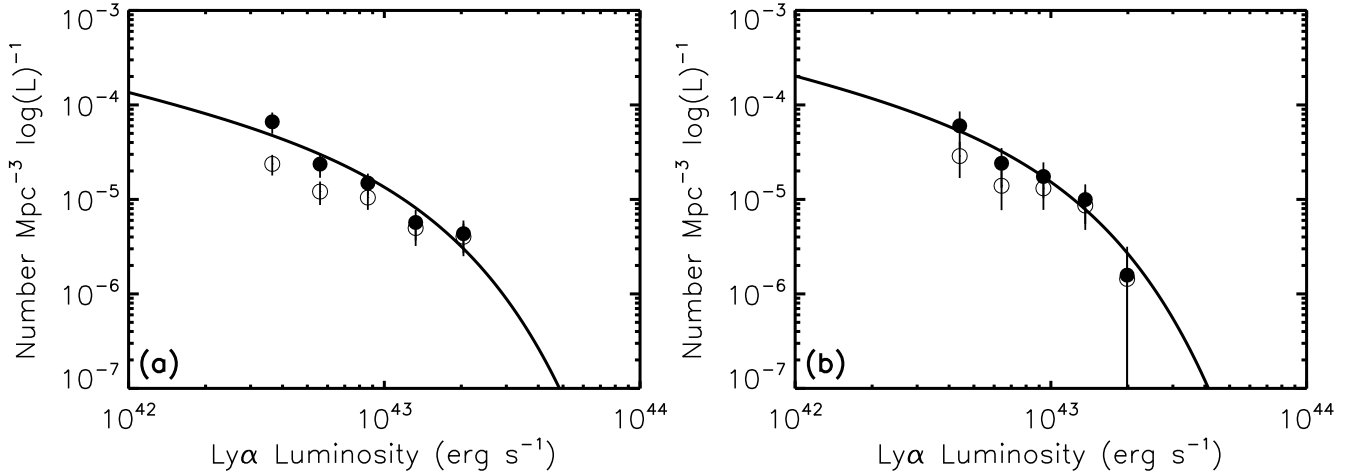


Figure 5. (a) Derived Ly α luminosity function at $z = 0.67 - 1.16$ for the LAE galaxies in deep *GALEX* grism fields (CDFS, GROTH, NGPDWS, and COSMOS) with $EW_r(\text{Ly}\alpha) \geq 20 \text{ \AA}$ from both the *GALEX* pipeline and the data cube samples (black circles: open—raw data; solid—corrected for the effects of incompleteness using the results from our Monte Carlo simulations). The black curve indicates the best fit Schechter function assuming a fixed slope of $\alpha = -1.6$. We find best fit parameters $\log L_* = 43.0 \pm 0.2$ and $\log \phi_* = -4.8 \pm 0.3$. (b) Same as Figure 5(a), but with the LAE survey limited to regions with deep X-ray data to ensure a robust AGN classification. Assuming a fixed slope of $\alpha = -1.6$, we find best fit Schechter parameters $\log L_* = 42.8 \pm 0.2$ and $\log \phi_* = -4.5 \pm 0.3$.

Table 3
Cumulative Luminosity Function

$\log(L)$ bin (erg s^{-1}) (1)	N (2)	$\frac{1}{\Delta \log(L)} \sum 1/V$ ($\text{Mpc}^{-3} \log(L)^{-1}$) (3)
42.468 - 42.655	17	$66.3 \pm 16.8 \times 10^{-6}$
42.655 - 42.842	13	$23.6 \pm 6.7 \times 10^{-6}$
42.842 - 43.029	15	$14.9 \pm 3.9 \times 10^{-6}$
43.029 - 43.216	8	$5.7 \pm 2.0 \times 10^{-6}$
43.216 - 43.403	7	$4.3 \pm 1.6 \times 10^{-6}$

and the Ly α LF in the luminosity range $L_1 \leq L_i \leq L_2$ and redshift range $z = 0.67 - 1.16$ is

$$LF = (\log(L_2) - \log(L_1))^{-1} \sum_{\{i: L_1 \leq L_i \leq L_2\}} 1/V_i.$$

In Figure 5(a), we show our raw LF (black open circles) along with our LF corrected for incompleteness (black solid circles). Error bars are $\pm 1\sigma$ Poisson errors. In Table 3 Columns 1, 2, and 3, we list the luminosity bins, the number of LAE galaxies per bin, and the computed luminosity function values corrected for incompleteness. We have tested that these results are not dependent on our method of constructing flux bins. Alternatively, for each field, we generated 5 flux bins of equal size within the range of f_{thres} to the maximum observed Ly α flux, where f_{thres} is the Ly α flux corresponding to 50% completeness (see Figure 2). This method reduces the dependence on our completeness simulations but does not significantly change our results.

We may correct for any remaining AGNs in our sample by restricting our field to regions with deep X-ray data. This removes the NGPDWS field and restricts the area of the remaining $50' \times 50'$ *GALEX* fields but ensures a robust AGN classification. In Figure 5(b), we show our X-ray data limited LF (black circles). Comparing this LF to the LF computed from the full LAE galaxy sample, we find that all points are consistent within 1σ error bars.

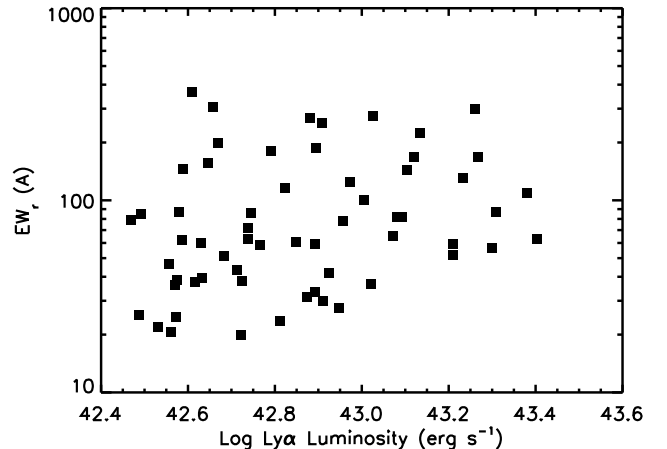


Figure 6. Rest-frame EWs vs. log Ly α luminosity for the full sample.

We find that our LAE galaxy LF is consistent with the $z \sim 1$ LAE galaxy LF computed in BCW12. BCW12 based their LF on ~ 20 LAE galaxies found in one of the four *GALEX* fields contained in this study. We have increased the sample size by a factor of three. Furthermore, we have searched for AGNs in the BCW12 LAE galaxy sample (none found) and removed spurious sources (3 BCW12 LAE candidates) with our newly obtained optical spectroscopic data.

5. DISTRIBUTION OF EQUIVALENT WIDTHS

In Figure 6, we show our rest-frame EWs versus redshift. Because we have a flux-limited sample, the distribution of these EWs should be directly comparable to narrowband Ly α selected samples at higher redshifts. In Figure 7(a), we show the distribution of these EWs for the full sample.

The rest-frame EW distribution is normally fit with an exponential function. For the LAE samples, which are truncated below 20 \AA , the maximum likelihood estimate of the scale length is the mean of the rest-frame EW values minus 20 \AA . We find a scale length of $80 \pm 10 \text{ \AA}$ for

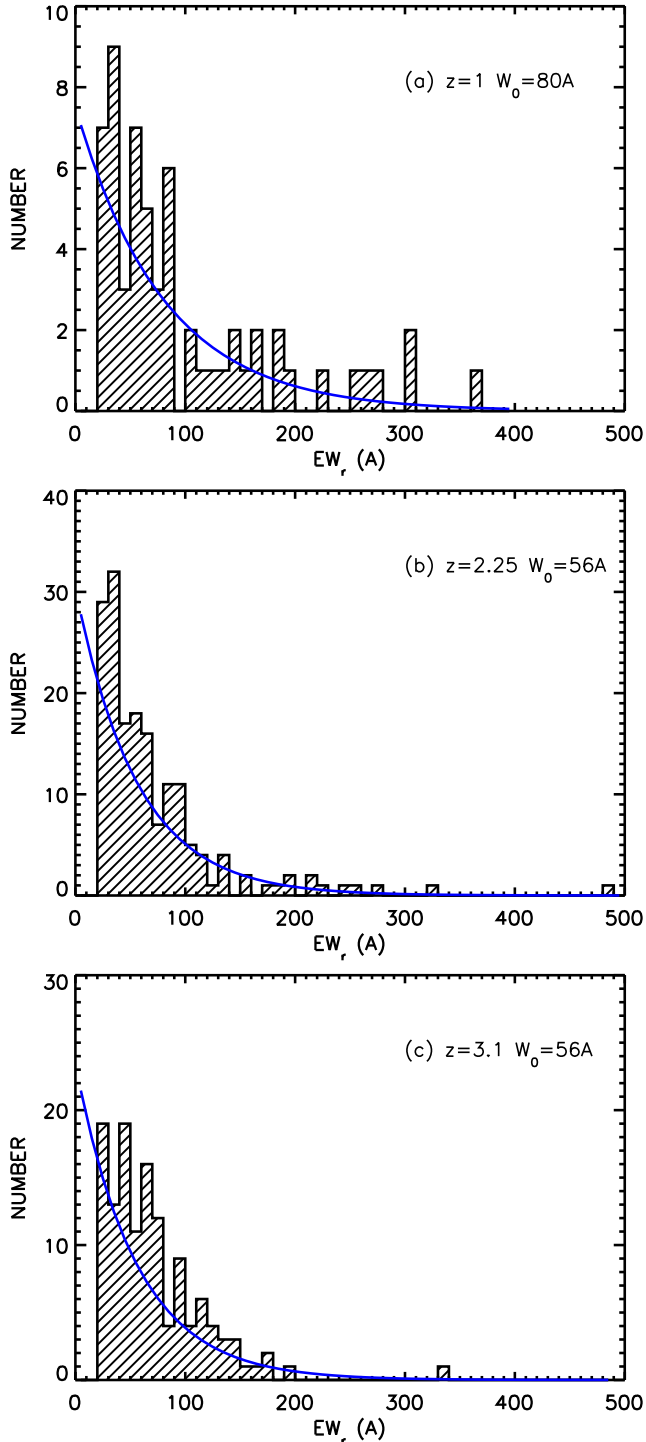


Figure 7. Histograms of the rest-frame EWs in 10 \AA bins. (a) The present sample at $z \sim 1$. (b) The Nilsson et al. (2009) sample at $z = 2.25$. (c) The Ciardullo et al. (2012) sample at $z = 3.1$. In each case, the blue curve shows the exponential distribution computed using a maximum likelihood procedure. The rest-frame scale length is $80 \pm 10 \text{ \AA}$ for $z \sim 1$, $56 \pm 7 \text{ \AA}$ for $z = 2.25$, and $56 \pm 7 \text{ \AA}$ for $z = 3.1$.

(A color version of this figure is available in the online journal.)

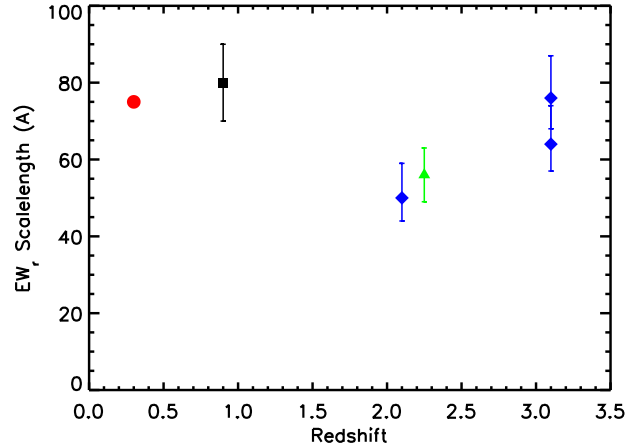


Figure 8. Maximum likelihood estimates of the rest-frame EW scale length from the present $z \sim 1$ sample (black square), the $z = 2.25$ Nilsson et al. (2009) sample (green triangle), and the $z = 2.1$ Guaita et al. (2010), $z = 3.1$ Gronwall et al. (2007), and $z = 3.1$ Ciardullo et al. (2012) samples (blue diamonds; values quoted from Ciardullo et al.) vs. redshift. The red circle shows the scale length from the $z = 0.3$ *GALEX* LAE sample of Cowie et al. (2010) after correction for their continuum selection, as described in their Section 5.4.

(A color version of this figure is available in the online journal.)

the full sample, where we computed the error using the parameterized bootstrap method. Separating the sample by luminosity gives a scale length of $91 \pm 14 \text{ \AA}$ for sources with logarithmic Ly α luminosities above 42.8 and $68 \pm 10 \text{ \AA}$ for those with lower luminosities. This is consistent with the distribution being invariant as a function of Ly α luminosity, as has been found in the higher redshift samples (Ciardullo et al. 2012).

We compare our sample at $z \sim 1$ with a sample at $z = 2.25$ from Nilsson et al. (2009) (Figure 7(b)) and a sample at $z = 3.1$ from Ciardullo et al. (2012) (Figure 7(c)). The Nilsson et al. sample has a logarithmic luminosity limit of 42.4 erg s^{-1} , which is very similar to that of the present sample, while the Ciardullo et al. sample covers 42 erg s^{-1} to just above 43 erg s^{-1} , making it slightly fainter, on average. The Nilsson et al. and Ciardullo et al. maximum likelihood estimates of the rest-frame EW scale length are both $56 \pm 7 \text{ \AA}$. Nilsson et al. also give a least squares fit value of $56 \pm 7 \text{ \AA}$, which is consistent within the errors.

However, when Ciardullo et al. (2012) allowed for biases in their sample, such as those introduced by the filter shape, then their rest-frame EW scale length rose to $64^{+10}_{-7} \text{ \AA}$. When Ciardullo et al. analyzed an alternate sample at $z = 3.1$ from Gronwall et al. (2007) in the same way, they found $76^{+11}_{-8} \text{ \AA}$. From the combined samples, they found 70^{+7}_{-5} \AA . Ciardullo et al. also reanalyzed the $z = 2.1$ sample from Guaita et al. (2010) in a self-consistent way and found 50^{+9}_{-6} \AA . The Ciardullo et al. $z = 2.1$ value is consistent with the Nilsson et al. (2009) $z = 2.25$ value. Based on an Anderson-Darling test, they concluded that there is a significant difference between the $z = 3.1$ and $z = 2.1$ samples.

The Ciardullo et al. (2012) analysis emphasizes that differences inherent in the methodology and fitting procedure are important. In particular, comparisons between the present sample, where the line fluxes are computed

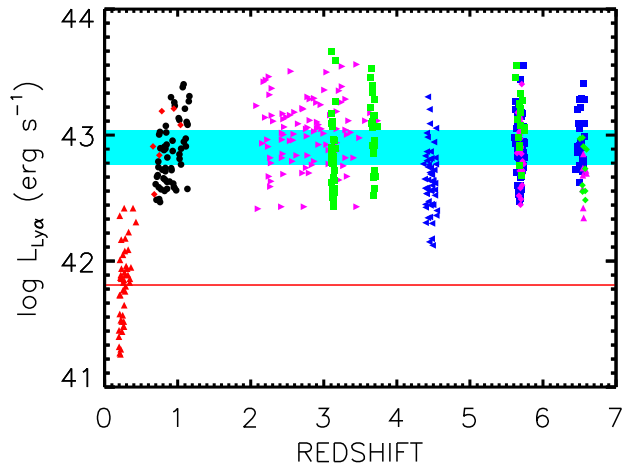


Figure 9. Observed Ly α luminosity vs. redshift for LAE galaxies with $\text{EW}_r(\text{Ly}\alpha) \geq 20 \text{ \AA}$. We show pipeline *GALEX* LAEs from Cowie et al. (2011, red triangles and red diamonds), data cube *GALEX* LAEs from this study (black circles), $z = 1.9 - 3.8$ HETDEX LAEs from Blanc et al. (2011, magenta right pointing triangles), $z = (3.1, 3.7, 5.7)$ LAEs from Ouchi et al. (2008, green squares), $z = 4.5$ LAEs from Dawson et al. (2007, blue left pointing triangles), $z = (5.7, 6.5)$ LAEs from Hu et al. (2010, blue squares), $z = 5.7$ LAEs from Shimasaku et al. (2006, magenta diamonds), and $z = 6.5$ LAEs from Taniguchi et al. (2005, green diamonds) and Kashikawa et al. (2006, magenta triangles). The red line shows the L_* derived for the $z \sim 0.3$ LF assuming a slope of $\alpha = -1.6$. The cyan area shows the range of L_* values derived for the $z = 2.85 - 5.7$ LFs.

(A color version of this figure is available in the online journal.)

from the spectra and the continua from the broadband magnitudes, and samples such as the Ciardullo et al. sample, which are based purely on imaging data, can be tricky (e.g., Zheng et al. 2013). Nevertheless, the present sample appears to indicate that, if there is indeed a narrowing of the rest-frame EW distribution from $z = 3$ to $z = 2$, then it has reversed by $z = 1$.

In Figure 8, we show the rest-frame EW scale lengths measured from the maximum likelihood procedures for the present sample (black square), the $z = 2.25$ Nilsson et al. (2009) sample (green triangle), and the $z = 2.1$ Guaita et al. (2010), $z = 3.1$ Ciardullo et al. (2012), and $z = 3.1$ Gronwall et al. (2007) samples (blue diamonds; values quoted from Ciardullo et al.). While there may be a drop at $z \sim 2$, overall the scale length shows little variation with redshift. This is in sharp contrast to the analysis of Zheng et al. (2013), who found a redshift evolution of $(1+z)^{1.7}$. The Zheng et al. result appears to be due primarily to their misinterpretation of the scale length given by Cowie et al. (2010) for their $z = 0.3$ *GALEX* LAE sample. Zheng et al. used 23.7 ± 2.2 , which was what Cowie et al. gave for their continuum selected sample. However, as Cowie et al. emphasized in their Section 5.4, this needs to be corrected for missing high EW sources before it can be compared with Ly α luminosity selected samples. In Figure 8, we show the Cowie et al. corrected scale length of 75 \AA (red circle). (Because of the large systematic errors, we do not show an error bar.) This is fully consistent with there being a constant value of the scale length with redshift.

6. DISCUSSION

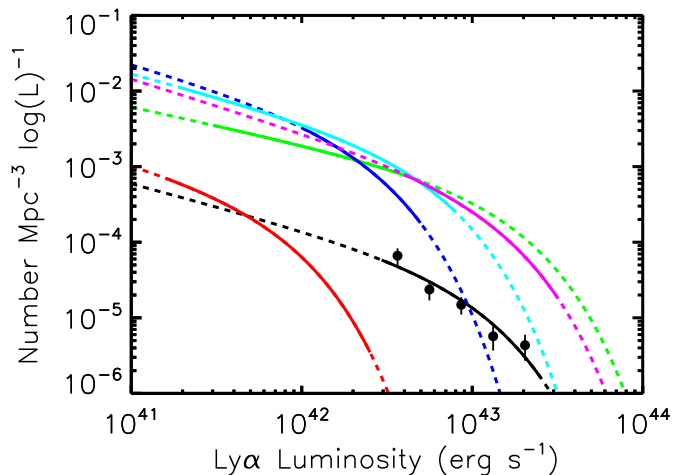


Figure 10. Derived Ly α luminosity function at $z = 0.67 - 1.16$ for the LAE galaxies in deep *GALEX* grism fields (black circles from Figure 5(a)) compared to other Ly α luminosity functions in close redshift proximity. The fitted Schechter functions are shown as solid curves over the extent of their observed data points. The black curve indicates our best fit Schechter function assuming a fixed slope of $\alpha = -1.6$. The red curve indicates the $z = 0.194 - 0.44$ Cowie et al. (2010) LF. The blue curve indicates the $z = 2.1$ Ciardullo et al. (2012) LF. The green curve indicates the $z = 2.2$ Hayes et al. (2010) LF. The cyan curve indicates the $z = 1.95 - 3$ Cassata et al. (2011) LF. The magenta curve indicates the $z = 1.9 - 3.8$ Blanc et al. (2011) LF.

(A color version of this figure is available in the online journal.)

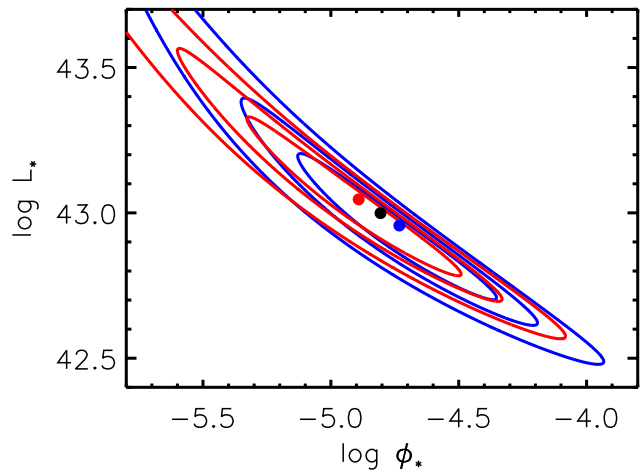


Figure 11. 1σ , 2σ , and 3σ contours for the $z \sim 1$ luminosity function parameters L_* and ϕ_* assuming a faint end slope of $\alpha = -1.5$ (blue) and $\alpha = -1.7$ (red). The blue, black, and red circles show our best fit Schechter function results for the full LAE galaxy sample assuming $\alpha = -1.5$ (blue circle), $\alpha = -1.6$ (black circle), and $\alpha = -1.7$ (red circle). Regardless of the assumed faint end slope, $\log L_* \phi_* \sim 38.2$.

(A color version of this figure is available in the online journal.)

In Figure 9, we show the dramatic increase in the observed Ly α luminosities to a redshift of $z \sim 1$ followed by relatively no luminosity evolution from $z \sim 1$ to $z \sim 6$. This large luminosity boost was previously noted by Cowie et al. (2011) with a sample of ~ 5 LAEs at a redshift of $z \sim 1$ (see Figure 9, red diamonds). We have now increased the sample size of $z \sim 1$ LAEs to 60 galaxies (see Figure 9, black circles). Our relatively nearby $z \sim 1$ sample will facilitate the study of LAEs with luminosities analogous to high-redshift LAEs. In Paper II,

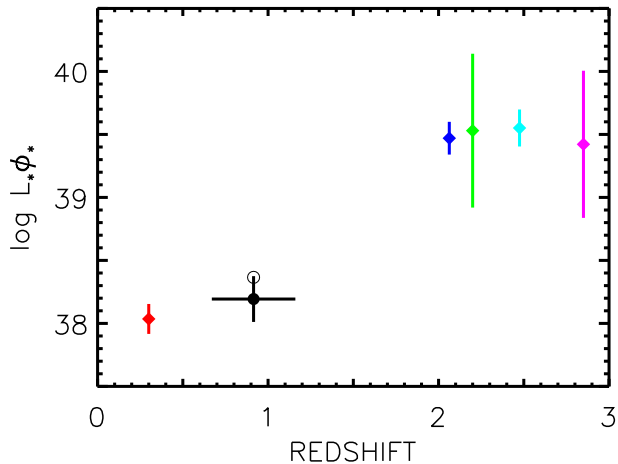


Figure 12. The product $L_*\phi_*$ vs. redshift for the LAE galaxy LFs shown in Figure 5. The black solid circle shows the product $L_*\phi_* = 38.2 \pm 0.2$ from our best fit $z \sim 1$ LAE galaxy LF. The black open circle shows the product $L_*\phi_* = 38.4 \pm 0.2$ from our fit to the $z \sim 1$ LAE galaxy LF limited to regions with deep X-ray data. Both $z \sim 1$ fits assume a faint end slope $\alpha = -1.6$. Error bars are estimated from the published uncertainties in L_* and ϕ_* . (A color version of this figure is available in the online journal.)

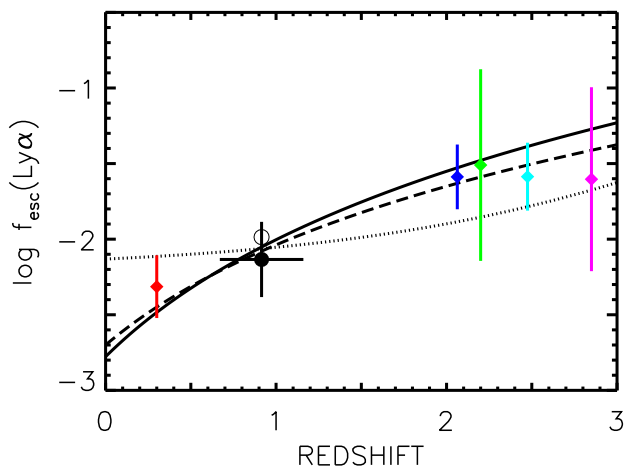


Figure 13. Sample averaged $\text{Ly}\alpha$ escape fractions for all LFs presented in Figure 5. The black solid circle shows $f_{esc}(\text{Ly}\alpha) = 0.7\% \pm 0.4\%$ computed from our best fit $z \sim 1$ LF. The black open circle shows $f_{esc}(\text{Ly}\alpha) = 1.0\% \pm 0.6\%$ computed from our fitted LF limited to regions with deep X-ray data. Diamonds (from low redshift to high) indicate $f_{esc}(\text{Ly}\alpha)$ derived from Cowie et al. (2010), Ciardullo et al. (2012), Hayes et al. (2010), Cassata et al. (2011), and Blanc et al. (2011). Error bars are estimated from the published uncertainties in L_* and ϕ_* . The solid and dashed black curves are from Hayes et al. (2011) and Blanc et al. (2011), respectively, and show the best fit power law to $f_{esc}(\text{Ly}\alpha)$ data. The dotted black curve shows the best fit transition model from Blanc et al. (2011). The calculated points and the selected curves have not been corrected for IGM absorption, which should be negligible at $z \sim 1$ and within the 1σ uncertainties at $z < 3$.

(A color version of this figure is available in the online journal.)

we will use the available spectroscopic and imaging data to constrain the properties of our sample and to serve as a baseline for studies of higher redshift LAEs.

In order to quantify the evolution in L_* , we have held the slope α fixed and found the best Schechter (1976) function fit to our data. We assume a slope of $\alpha = -1.6$, which allows us to compare directly our results to the LAE galaxy LF at $z \sim 0.3$ ($\alpha = -1.6$, $\log L_* = 41.81 \pm$

0.09 , $\log \phi_* = -3.77 \pm 0.08$; Cowie et al. 2010). We obtain $\log L_* = 43.0 \pm 0.2$ and $\log \phi_* = -4.8 \pm 0.3$ (see Figure 5(a)). Limiting our sample to regions with deep X-ray data, we obtain $\log L_* = 42.8 \pm 0.2$ and $\log \phi_* = -4.5 \pm 0.3$ (see Figure 5(b)).

Both our $L_*(z \sim 1)$ values are roughly consistent with L_* values found for LAE galaxy LFs at $z \sim 3$ ($\log L_* = 42.7$, Gronwall et al. 2007; $\log L_* = 42.8$, Ouchi et al. 2008; $\log L_* = 42.8$, Ciardullo et al. 2012) and imply an L_* increase by a factor of ~ 15 from $z \sim 0.3$ to $z \sim 1$ (from $\log L_*(z \sim 0.3) = 41.81 \pm 0.09$ to $\log L_*(z \sim 1) = 43.0 \pm 0.2$). A large boost in L_* is in agreement with the evolution seen in other LFs tracing star-forming galaxies. Both $\text{H}\alpha$ and UV LFs are found to be dominated by luminosity evolution over the redshift range $z \sim 0.3 - 2$. Sobral et al. (2013) investigated $\text{H}\alpha$ LFs and found that $L_*(\text{H}\alpha)$ increases by a factor of 10 from $z \sim 0$ to $z \sim 2$. Oesch et al. (2010) investigated UV LFs and found that $L_*(\text{UV})$ increases by a factor of ~ 16 from $z \sim 0$ to $z \sim 3$.

However, our fitted Schechter parameters indicate a decrease in ϕ_* from $z \sim 0.3$ to $z \sim 1$ (from $\log \phi_*(z \sim 0.3) = -3.77 \pm 0.08$ to $\log \phi_*(z \sim 1) = -4.8 \pm 0.3$). It is only beyond $z \sim 1$ that there is a significant increase in ϕ_* . Referring again to other LFs tracing star-forming galaxies, we note that, unlike L_* , ϕ_* does not increase monotonically over the redshift range $z \sim 0.3 - 2$. Within the uncertainties of their measurements, both Sobral et al. (2013, for $\phi_*(\text{H}\alpha)$) and Oesch et al. (2010, for $\phi_*(\text{UV})$) found very little evidence for ϕ_* evolution from $z \sim 0$ to $z \sim 2$. As discussed in more detail below, we find that our best fit Schechter functions with higher L_* values tend to have lower ϕ_* values. Given this issue and the poorly constrained faint end slope, a clearer picture of the evolution of individual Schechter function parameters awaits a $z \sim 1$ LAE survey probing lower $\text{Ly}\alpha$ luminosities. Such a survey is not possible with currently available telescopes but would allow stronger constraints on the $L_*(z \sim 1)$ and $\phi_*(z \sim 1)$ values.

In Figure 10, we compare our $z \sim 1$ LF computed from the full LAE galaxy sample to other $\text{Ly}\alpha$ luminosity functions in close redshift proximity. We show the fitted Schechter functions as solid lines over the extent of their observed data points. For the $z \sim 2$ Schechter function parameters, the $\log L_*$ values range from 42.3 to 43.2, the $\log \phi_*$ values range from -3.7 to -2.9 , and the α values range from -1.7 to -1.5 (see the blue, green, cyan, and magenta lines in Figure 10). Due to the differing survey volumes and fitting assumptions, it is still possible that all $z \sim 2$ data are in overall agreement (Blanc et al. 2011; Ciardullo et al. 2012).

The Schechter function parameters ϕ_* and L_* are known to be strongly correlated, while assuming different values of α tends to leave the product $L_*\phi_*$ unchanged. We show this for our Schechter function fit in Figure 11. For these reasons, we consider the product $L_*\phi_*$ and the luminosity density, which is proportional to $L_*\phi_*$, to be more reliable than the values of individual Schechter parameters. In Figure 12, we show that a coherent picture emerges by comparing our results to the $L_*\phi_*$ values found in the literature. As noted by Blanc et al. (2011), there is a trend (in agreement with our uncertainty contours) for the $z \sim 2$ Schechter function fits with higher L_* values to have lower ϕ_* values. Thus, the $z \sim 2$ Schechter functions — which have L_* values that differ by about

an order of magnitude — are found to have consistent $L_*\phi_*$ values. The product $L_*\phi_*$ increases by a factor of ~ 1.5 from $z \sim 0.3$ to $z \sim 1$ followed by an increase by a factor of ~ 20 from $z \sim 1$ to $z \sim 2$.

The observed Ly α luminosity density provides an estimate of the total amount of Ly α light emitted by galaxies per unit volume:

$$\rho_{Ly\alpha}^{obs} = \int L\Phi(L)dL,$$

where $\Phi(L)$ is a Ly α Schechter function. Integrating this expression from 0 to $+\infty$ gives

$$\rho_{Ly\alpha}^{obs} = L_*\phi_*\Gamma(\alpha + 2),$$

where Γ is the Gamma function. The main source of uncertainty in this expression comes from the poorly constrained faint end slope α . Taking the extreme values for the $z \sim 2$ Schechter functions, $\alpha = -1.7$ and $\alpha = -1.5$, we find that Γ changes by a factor of 1.7. Modulo this factor, the evolution of the product $L_*\phi_*$ seen in Figure 12 from $z \sim 0.3$ to $z \sim 2$ results from the change in observed Ly α luminosity density.

To first order, the intrinsic production of Ly α photons in a galaxy is proportional to the SFR (Kennicutt 1998; Schaerer 2003). Thus, an overall increase in the Ly α luminosity density from $z \sim 0.3$ to $z \sim 2$ is expected due to the well established increase in the cosmic SFR density. However, observed Ly α luminosities will significantly deviate from intrinsic Ly α luminosities due to resonant scattering of Ly α photons by neutral hydrogen.

To quantify this, we calculate the $z \sim 1$ volumetric Ly α escape fraction, $f_{esc}(Ly\alpha)$, and compare its value to other measurements taken at nearby redshifts. The volumetric Ly α escape fraction measures the fraction of Ly α photons that escape from the survey volume. We emphasize that its value will be systematically lower than the Ly α escape fractions derived for individual LAEs. For example, Blanc et al. (2011) find a $\sim 30\%$ median Ly α escape fraction for their $z = 1.9 - 3.8$ LAE sample but only a $\sim 3\%$ volumetric Ly α escape fraction.

The volumetric escape fraction is defined as the observed Ly α luminosity density divided by the intrinsic Ly α luminosity density,

$$f_{esc}(Ly\alpha) = \rho_{Ly\alpha}^{obs} / \rho_{Ly\alpha}^{int},$$

where the intrinsic Ly α luminosity density is found by taking a measure of the cosmic SFR density and then converting SFR to Ly α luminosity,

$$\rho_{Ly\alpha}^{int} = \rho_{SFR}(8.7)(1.26 \times 10^{41}).$$

The conversion factors come from the assumption of case B recombination (Brocklehurst 1971) and the SFR to H α Kennicutt (1998) relation. For consistency with Blanc et al. (2011), we integrate the Ly α LFs down to a $2.66 \times 10^{41} \text{erg s}^{-1}$ limit and obtain cosmic SFR density measurements from Bouwens et al. (2010). Blanc et al. (2011) estimate that the choice of the luminosity integration limit may alter the computed luminosity density by at most 60% (for further discussion of this issue see Hayes et al. 2011). Bouwens et al. (2010) derive cosmic SFR densities from extinction corrected rest-frame UV

LFs. We do not attempt to correct for IGM absorption, which should be negligible for our $z \sim 1$ sample.

Both Hayes et al. (2011) and Blanc et al. (2011) have compiled measurements from various Ly α LF studies spanning a redshift range of $z = 0.3 - 7.7$ to determine the evolution of $f_{esc}(Ly\alpha)$. Both groups fit power laws to these data and find evidence for a rapidly increasing $f_{esc}(Ly\alpha)$, which approaches 100% at high redshifts ($z \sim 9$).

We find a $z \sim 1$ $f_{esc}(Ly\alpha)$ of $0.7\% \pm 0.4\%$. In Figure 5, we show that the $f_{esc}(Ly\alpha)$ computed from our best fit $z \sim 1$ Schechter function is consistent with the $f_{esc}(Ly\alpha)$ value of $\sim 0.9\%$ interpolated from the power law fits of Hayes et al. (2011) and Blanc et al. (2011). In Figure 5, we also show $f_{esc}(Ly\alpha) = 1.0\% \pm 0.6\%$ (open circle) computed from our fitted LF limited to regions with deep X-ray data. Hayes et al. (2011) argue that the rising trend in the volumetric Ly α escape fraction with increasing redshift is consistent with expectations due to the general decline of dust content in star-forming galaxies. We have now constrained the $f_{esc}(Ly\alpha)$ from $z \sim 0.3$ to $z \sim 2$ and find results consistent with this inferred trend.

7. SUMMARY

We presented a catalog of 135 candidate $z \sim 1$ LAEs. We obtained optical spectral data for 90% of our sample. We found that only $\sim 13\%$ of our sample are either spurious, stars, or strong CIV $\lambda 1549$ emitters. Combining these optical data with the UV spectra and X-ray imaging data, we found that 49% of our Ly α emitters are AGNs. Eliminating AGNs and LAEs with $EW_r(Ly\alpha) < 20 \text{ \AA}$ gives a final sample of 60 star-forming LAEs, which we used to compute the $z \sim 1$ Ly α LF and the $z \sim 1$ Ly α volumetric escape fraction ($f_{esc}(Ly\alpha) = 0.7\% \pm 0.4\%$). We note that no improved $z \sim 1$ Ly α LFs are possible for the foreseeable future due to the lack of UV telescopes. Our best fit LF implies a significant increase in L_* between $z \sim 0.3$ and $z \sim 1$ without much change in the luminosity density. This requires a rapid increase in ϕ_* between $z \sim 1$ and $z \sim 2$. It is clear that the intrinsic properties of the LAEs must be changing rapidly in the $z \sim 1 - 2$ interval, resulting in a rapid increase in the Ly α escape fraction. Our cataloged sources offer the best opportunity to study emitters with luminosities comparable to LAEs found in the early universe. With the optical data in hand, Paper II will compare our sample's physical properties to a UV-selected control sample.

We would like to thank the referee for their critical reading of the paper and useful suggestions for improving it. We gratefully acknowledge support from a NASA Keck PI Data Award, administered by the NASA Exoplanet Science Institute, a Wisconsin Space Grant Consortium Graduate Fellowship, and a Sigma Xi Grant in Aid of Research Award (I.G.B.W.). We also appreciate support from the University of Wisconsin Research Committee with funds granted by the Wisconsin Alumni Research Foundation and the David and Lucile Packard Foundation (A.J.B.), as well as from NSF grant AST-0709356 (L.L.C.). We thank Michael Cooper for supplying spectra from the Arizona CDFS Environment Survey

(ACES). This research has made use of the NASA/IPAC Extragalactic Database (NED), which is operated by the Jet Propulsion Laboratory, California Institute of Technology, under contract with the National Aeronautics and Space Administration.

REFERENCES

- Alexander, D. M., Bauer, F. E., Brandt, W. N., et al. 2003, *AJ*, 126, 539
- Atek, H., Kunth, D., Schaerer, D., et al. 2009, *A&A*, 506, L1
- Atek, H., Siana, B., Scarlata, C., et al. 2011, *ApJ*, 743, 121
- Barger, A. J., Cowie, L. L., Brandt, W. N., et al. 2002, *AJ*, 124, 1839
- Barger, A. J., Cowie, L. L., & Wold, I. G. B. 2012, *ApJ*, 749, 106
- Bertin, E., & Arnouts, S. 1996, *A&AS*, 117, 393
- Blanc, G. A., Adams, J. J., Gebhardt, K., et al. 2011, *ApJ*, 736, 31
- Bouwens, R. J., Illingworth, G. D., Oesch, P. A., et al. 2010, *ApJ*, 709, L133
- Brocklehurst, M. 1971, *MNRAS*, 153, 471
- Burgh, E. B., Nordsieck, K. H., Koblunicky, H. A., et al. 2003, in *Society of Photo-Optical Instrumentation Engineers (SPIE) Conference Series*, Vol. 4841, *Society of Photo-Optical Instrumentation Engineers (SPIE) Conference Series*, ed. M. Iye & A. F. M. Moorwood, 1463–1471
- Cardelli, J. A., Clayton, G. C., & Mathis, J. S. 1989, *ApJ*, 345, 245
- Cassata, P., Le Fèvre, O., Garilli, B., et al. 2011, *A&A*, 525, A143
- Ciardullo, R., Gronwall, C., Wolf, C., et al. 2012, *ApJ*, 744, 110
- Cooper, M. C., Yan, R., Dickinson, M., et al. 2012, *MNRAS*, 425, 2116
- Cowie, L. L., Barger, A. J., & Hu, E. M. 2010, *ApJ*, 711, 928
- . 2011, *ApJ*, 738, 136
- Cowie, L. L., Songaila, A., Hu, E. M., & Cohen, J. G. 1996, *AJ*, 112, 839
- Dawson, S., Rhoads, J. E., Malhotra, S., et al. 2007, *ApJ*, 671, 1227
- Deharveng, J.-M., Small, T., Barlow, T. A., et al. 2008, *ApJ*, 680, 1072
- Elvis, M., Civano, F., Vignali, C., et al. 2009, *ApJS*, 184, 158
- Faber, S. M., Phillips, A. C., Kibrick, R. I., et al. 2003, in *Society of Photo-Optical Instrumentation Engineers (SPIE) Conference Series*, Vol. 4841, *Society of Photo-Optical Instrumentation Engineers (SPIE) Conference Series*, ed. M. Iye & A. F. M. Moorwood, 1657–1669
- Felten, J. E. 1976, *ApJ*, 207, 700
- Finkelstein, S. L., Rhoads, J. E., Malhotra, S., & Grogin, N. 2009, *ApJ*, 691, 465
- Finkelstein, S. L., Rhoads, J. E., Malhotra, S., Pirzkal, N., & Wang, J. 2007, *ApJ*, 660, 1023
- Fitzpatrick, E. L. 1999, *PASP*, 111, 63
- Gawiser, E., Francke, H., Lai, K., et al. 2007, *ApJ*, 671, 278
- Giavalisco, M., Ferguson, H. C., Koekemoer, A. M., et al. 2004, *ApJ*, 600, L93
- Greig, B., Komatsu, E., & Wyithe, J. S. B. 2013, *MNRAS*, 431, 1777
- Grogin, N. A., Kocevski, D. D., Faber, S. M., et al. 2011, *ApJS*, 197, 35
- Gronwall, C., Ciardullo, R., Hickey, T., et al. 2007, *ApJ*, 667, 79
- Guaia, L., Gawiser, E., Padilla, N., et al. 2010, *ApJ*, 714, 255
- Hayes, M., Schaerer, D., Östlin, G., et al. 2011, *ApJ*, 730, 8
- Hayes, M., Östlin, G., Schaerer, D., et al. 2010, *Nature*, 464, 562
- Hill, G. J., Gebhardt, K., Komatsu, E., et al. 2008, in *Astronomical Society of the Pacific Conference Series*, Vol. 399, *Panoramic Views of Galaxy Formation and Evolution*, ed. T. Kodama, T. Yamada, & K. Aoki, 115
- Hornschemeier, A. E., Brandt, W. N., Garmire, G. P., et al. 2001, *ApJ*, 554, 742
- Hu, E. M., Cowie, L. L., Barger, A. J., et al. 2010, *ApJ*, 725, 394
- Hu, E. M., Cowie, L. L., & McMahon, R. G. 1998, *ApJ*, 502, L99
- Kashikawa, N., Shimasaku, K., Malkan, M. A., et al. 2006, *ApJ*, 648, 7
- Kennicutt, Jr., R. C. 1998, *ApJ*, 498, 541
- Kenter, A., Murray, S. S., Forman, W. R., et al. 2005, *ApJS*, 161, 9
- Koekemoer, A. M., Faber, S. M., Ferguson, H. C., et al. 2011, *ApJS*, 197, 36
- Kornei, K. A., Shapley, A. E., Erb, D. K., et al. 2010, *ApJ*, 711, 693
- Kunth, D., Leitherer, C., Mas-Hesse, J. M., Östlin, G., & Petrosian, A. 2003, *ApJ*, 597, 263
- Lai, K., Huang, J.-S., Fazio, G., et al. 2008, *ApJ*, 674, 70
- Laird, E. S., Nandra, K., Georgakakis, A., et al. 2009, *ApJS*, 180, 102
- Laursen, P., Sommer-Larsen, J., & Razoumov, A. O. 2011, *ApJ*, 728, 52
- Leauthaud, A., Massey, R., Kneib, J.-P., et al. 2007, *ApJS*, 172, 219
- Lehmer, B. D., Brandt, W. N., Alexander, D. M., et al. 2005, *ApJS*, 161, 21
- Lilly, S. J., Le Fèvre, O., Renzini, A., et al. 2007, *ApJS*, 172, 70
- Luo, B., Bauer, F. E., Brandt, W. N., et al. 2008, *ApJS*, 179, 19
- Markwardt, C. B. 2009, in *Astronomical Society of the Pacific Conference Series*, Vol. 411, *Astronomical Data Analysis Software and Systems XVIII*, ed. D. A. Bohlender, D. Durand, & P. Dowler, 251
- Martin, D. C., Fanson, J., Schiminovich, D., et al. 2005, *ApJ*, 619, L1
- Morrissey, P., Conrow, T., Barlow, T. A., et al. 2007, *ApJS*, 173, 682
- Neufeld, D. A. 1991, *ApJ*, 370, L85
- Newman, J. A., Cooper, M. C., Davis, M., et al. 2012, *ArXiv e-prints*
- Nilsson, K. K., & Møller, P. 2011, *A&A*, 527, L7
- Nilsson, K. K., Tapken, C., Møller, P., et al. 2009, *A&A*, 498, 13
- Nilsson, K. K., Møller, P., Møller, O., et al. 2007, *A&A*, 471, 71
- Oesch, P. A., Bouwens, R. J., Carollo, C. M., et al. 2010, *ApJ*, 725, L150
- Östlin, G., Hayes, M., Kunth, D., et al. 2009, *AJ*, 138, 923
- Ouchi, M., Shimasaku, K., Akiyama, M., et al. 2008, *ApJS*, 176, 301
- Popesso, P., Dickinson, M., Nonino, M., et al. 2009, *A&A*, 494, 443
- Rix, H.-W., Barden, M., Beckwith, S. V. W., et al. 2004, *ApJS*, 152, 163
- Scarlata, C., Colbert, J., Teplitz, H. I., et al. 2009, *ApJ*, 704, L98
- Schaerer, D. 2003, *A&A*, 397, 527
- Schaerer, D., & de Barros, S. 2009, *A&A*, 502, 423
- Schaerer, D., & Verhamme, A. 2008, *A&A*, 480, 369
- Schechter, P. 1976, *ApJ*, 203, 297
- Schlafly, E. F., & Finkbeiner, D. P. 2011, *ApJ*, 737, 103
- Shapley, A. E., Steidel, C. C., Pettini, M., & Adelberger, K. L. 2003, *ApJ*, 588, 65
- Shimasaku, K., Kashikawa, N., Doi, M., et al. 2006, *PASJ*, 58, 313
- Silverman, J. D., Mainieri, V., Salvato, M., et al. 2010, *ApJS*, 191, 124
- Sobral, D., Smail, I., Best, P. N., et al. 2013, *MNRAS*, 428, 1128
- Stark, D. P., Ellis, R. S., & Ouchi, M. 2011, *ApJ*, 728, L2
- Szokoly, G. P., Bergeron, J., Hasinger, G., et al. 2004, *ApJS*, 155, 271
- Taniguchi, Y., Ajiki, M., Nagao, T., et al. 2005, *PASJ*, 57, 165
- Treister, E., Virani, S., Gawiser, E., et al. 2009, *ApJ*, 693, 1713
- Trump, J. R., Impey, C. D., Elvis, M., et al. 2009, *ApJ*, 696, 1195
- Vanzella, E., Cristiani, S., Dickinson, M., et al. 2008, *A&A*, 478, 83
- Virani, S. N., Treister, E., Urry, C. M., & Gawiser, E. 2006, *AJ*, 131, 2373
- Zheng, Z.-Y., Wang, J.-X., Malhotra, S., et al. 2013, *ArXiv e-prints*

Table 4
Emission-line Sample: CDFS-00

Name	R.A.	Decl.	NUV	FUV	z_{galax}	$\log L(\text{Ly}\alpha)$	$\text{EW}_r(\text{Ly}\alpha)$	$\log f_{2-8}^a$	Type(UV)	R.A.(opt)	Decl.(opt)	Offset	z_{opt}	Type(opt)
(1)	(J2000.0)	(J2000.0)	(AB)	(AB)	(6)	(erg s^{-1})	(\AA)	($\text{erg cm}^{-2}\text{s}^{-1}$)	(10)	(J2000.0)	(J2000.0)	(arcsec)	(14)	(15)
GALEX033111-281725 ⁱ	52.796374	-28.290444	23.55	27.50	1.168	43.61	281±17	52.796253	-28.290321	0.6	1.164 ^b	AGN
GALEX033112-281517	52.800377	-28.254936	23.02	28.01	1.162	43.31	87±5	52.800663	-28.255022	1.0	1.161 ^{b,c}	...
GALEX033359-275326	53.499160	-27.890792	22.04	24.13	1.143	43.53	63±2	...	AGN	53.499096	-27.890846	0.3	1.133 ^b	AGN
GALEX033301-273227	53.255196	-27.540939	23.45	-27.75	1.135	43.08	82±7	53.255268	-27.540880	0.3	1.136 ^b	...
GALEX033146-272942	52.942574	-27.495223	22.73	25.44	1.137	52.942543	-27.495167	0.3	(0.629) ^{b,g}	...
GALEX033348-280216	53.453649	-28.038008	23.40	25.53	1.128	43.09	82±8	53.453671	-28.038050	0.2	1.130 ^b	...
GALEX033230-280804	53.125683	-28.134514	22.34	23.83	1.124	43.27	47±3	...	AGN
GALEX033120-274917	52.837504	-27.821383	22.82	32.73	1.116	42.91	30±5	52.837444	-27.821638	0.9	1.113 ^b	...
GALEX033255-281320	53.231551	-28.222466	22.46	-27.50	1.087	42.95	28±3	53.231567	-28.222486	0.1	1.085 ^b	...
GALEX033112-281442 ⁱ	52.803095	-28.245108	22.19	-28.20	1.055	42.85	19±3	...	AGN	52.801987	-28.244835	3.6	1.042 ^b	...
GALEX033413-275940 ⁱ	53.555847	-27.994665	24.21	26.59	1.052	42.78	118±12	53.555477	-27.994663	1.2	1.051 ^b	AGN
GALEX033212-274913 ⁱ	53.051599	-27.820316	22.68	27.04	1.053	42.89	33±4	53.051613	-27.820168	0.5	1.048 ^b	...
GALEX033200-274319	53.001430	-27.722033	22.40	24.39	1.042	43.25	59±4	-14.2	...	53.001520	-27.722071	0.3	1.041 ^d	AGN
GALEX033228-273614	53.121022	-27.604317	23.62	26.66	1.036	42.77	59±9	53.118469	-27.604019	8.2	1.046 ^b	...
GALEX033113-274949	52.807630	-27.830242	22.45	31.95	1.031	42.81	24±3	52.807545	-27.830231	0.3	1.026 ^b	...
GALEX033331-280625 ⁱ	53.382523	-28.107164	24.41	27.66	1.029	42.80	141±14	53.382084	-28.106623	2.4	1.026 ^b	AGN
GALEX033202-280320	53.010734	-28.055702	23.44	25.22	1.018	42.94	81±6	-13.7	AGN	53.010658	-28.055834	0.5	1.015 ^b	AGN
GALEX033111-275506	52.798577	-27.918436	23.81	-27.52	1.010	43.12	168±17	52.798473	-27.918442	0.3	1.023 ^b	...
GALEX033336-274224	53.402806	-27.706674	23.02	26.37	0.977	43.22	119±6	-14.8	AGN	53.402771	-27.706703	0.2	0.976 ^b	...
GALEX033204-273725	53.017064	-27.623785	22.78	24.25	0.977	43.36	133±8	-13.6	AGN	53.016788	-27.623751	0.9	0.970 ^e	AGN
GALEX033246-274154	53.195680	-27.698408	23.17	26.61	0.976	43.20	128±10	53.196271	-27.698547	2.1	no z	...
GALEX033342-274035 ⁱ	53.425620	-27.676525	24.73	26.03	0.956	42.59	146±15	53.425163	-27.676567	1.5	0.948 ^b	...
GALEX033335-273934	53.398183	-27.659591	22.54	23.31	0.949	-14.3	...	53.398163	-27.659760	0.6	(0.622) ^b	...
GALEX033329-280127	53.373274	-28.024282	23.16	25.95	0.942	42.62	37±6	53.373272	-28.024244	0.1	0.940 ^b	...
GALEX033206-281408	53.026465	-28.235703	21.79	25.75	0.913	43.30	56±3	53.026493	-28.235905	0.7	0.909 ^b	...
GALEX033044-280237	52.686897	-28.043707	23.25	26.58	0.869	42.82	116±13	52.686813	-28.043819	0.5	0.859 ^{b,c}	...
GALEX033042-274215 ⁱ	52.679011	-27.704257	23.03	25.18	0.861	42.57	38±4	52.678730	-27.704462	1.2	0.856 ^b	...
GALEX033409-280129 ⁱ	53.541285	-28.024923	23.34	26.40	0.857	42.63	60±6	53.540737	-28.024443	2.5	0.854 ^b	...
GALEX033251-280809	53.214351	-28.135966	22.70	26.17	0.838	42.71	43±4	53.214489	-28.136051	0.5	0.832 ^b	...
GALEX033314-274834	53.310626	-27.809526	24.23	25.48	0.830	42.65	155±21	53.310975	-27.809095	1.9	0.826 ^d	...
GALEX033045-274506	52.689797	-27.751818	23.04	25.67	0.832	42.74	63±6	52.689950	-27.752197	1.4	no z ^h	...
GALEX033405-275023 ⁱ	53.521292	-27.839993	23.13	25.03	0.825	42.56	47±9	53.520832	-27.839972	1.5	0.821 ^b	...
GALEX033057-273316	52.739776	-27.554542	22.37	24.09	0.794	42.73	38±3	52.739708	-27.554583	0.3	0.790 ^b	...
GALEX033124-275625	52.851698	-27.940441	22.69	25.82	0.778	42.57	36±4	52.851761	-27.940475	0.2	0.773 ^b	...
GALEX033235-274059	53.148932	-27.683184	23.67	25.70	0.745	42.79	182±15	53.149258	-27.683273	1.1	0.735 ^b	...
GALEX033146-274846	52.942503	-27.812779	22.98	25.88	0.742	42.75	86±6	52.942345	-27.812771	0.5	0.736 ^b	...
GALEX033100-273020 ⁱ	52.751186	-27.505665	22.52	24.80	0.733	42.68	51±5	52.750877	-27.505367	1.5	0.727 ^b	...
GALEX033131-273429	52.880399	-27.574774	22.56	25.77	0.695	43.28	280±11	-14.1	...	52.880260	-27.574841	0.5	0.688 ^f	AGN
GALEX033321-275031 ⁱ	53.341285	-27.842052	23.16	25.06	0.691	42.59	90±9	...	AGN
GALEX033150-274116 ⁱ	52.962287	-27.687773	22.28	23.15	0.673	42.70	54±5	-14.2	AGN	52.962346	-27.687700	0.3	0.667 ^d	...

Note. —

^a X-ray data from Lehmer et al. (2005)

^b This paper's DEIMOS spectra

^c This paper's SALT spectra

^d Redshifts from Cooper et al. (2012)

^e Treister et al. (2009); Szokoly et al. (2004) give $z = 0.977$

^f Silverman et al. (2010)

^g [alt] Alternative counterpart at 52.942825, -27.494650, 2.2, (1.191)^b (R.A., Decl., Offset, z_{opt})

^h [alt] Two untargeted counterparts $\sim 2''$ from NUV position

ⁱ LAE candidate not listed in BCW12

Table 5
Emission-line Sample: GROTH-00

Name	R.A.	Decl.	NUV	FUV	z_{galax}	$\log L(\text{Ly}\alpha)$	$\text{EW}_{\text{r}}(\text{Ly}\alpha)$	$\log f_{2-10}^{\text{a}}_{\text{keV}}$	Type(UV)	R.A.(opt)	Decl.(opt)	Offset	z_{opt}	Type(opt)
(1)	(J2000.0) (2)	(J2000.0) (3)	(AB) (4)	(AB) (5)	(6)	(erg s^{-1}) (7)	(\AA) (8)	($\text{erg cm}^{-2}\text{s}^{-1}$) (9)	(10)	(J2000.0) (11)	(J2000.0) (12)	(arcsec) (13)	(14)	(15)
GALEX142028+524640	215.11946	52.777836	23.41	26.75	1.131	42.57	25±4	215.11989	52.777527	1.5	1.134 ^b	...
GALEX141814+524415	214.56075	52.737531	23.97	-27.83	1.128	43.10	144±14	214.56084	52.737473	0.3	1.123 ^b	...
GALEX141950+522542	214.96249	52.428532	24.09	26.34	1.114	42.97	124±12	214.96179	52.427998	2.5	1.111 ^b	...
GALEX142013+524008	215.05510	52.669118	25.11	29.17	1.100	43.05	380±49	215.05558	52.669342	1.2	no z ^d	...
GALEX141842+522919	214.67858	52.488791	22.69	23.68	1.084	42.98	37±5	-14.3	...	214.67863	52.488586	0.7	1.084 ^b	AGN
GALEX141824+522329	214.60416	52.391463	23.51	24.99	1.083	43.12	110±12	-13.6	...	214.60379	52.391666	1.1	1.081 ^b	AGN
GALEX141718+525521	214.32734	52.922402	22.47	24.41	1.067	43.58	127±4	...	AGN	214.32666	52.922764	2.0	1.064 ^b	AGN
GALEX142028+522516	215.12077	52.421360	23.00	26.88	1.052	42.94	51±4	215.12045	52.421455	0.8	1.045 ^b	AGN
GALEX141842+523735	214.67549	52.626454	23.07	25.43	1.038	43.17	93±14	214.67545	52.625916	1.9	1.035 ^b	AGN
GALEX141737+524236	214.40603	52.709992	22.20	26.33	1.027	43.53	99±6	-13.3	...	214.40543	52.710182	1.5	1.025 ^c	AGN
GALEX141815+530452	214.56554	53.081148	22.36	23.26	1.028	43.07	41±3	214.56442	53.081223	2.4	1.020 ^b	AGN
GALEX142015+525024	215.06357	52.840222	24.04	-28.66	1.021	43.13	223±20	215.06401	52.840656	1.8	1.014 ^b	...
GALEX142144+523627	215.43607	52.607699	21.83	24.66	1.011	43.32	46±3	215.43503	52.607677	2.3	1.006 ^b	AGN
GALEX142027+530455	215.11514	53.081989	23.18	-27.68	1.002	42.82	54±6	-13.1	...	215.11458	53.081806	1.4	0.994 ^b	AGN
GALEX141851+523600	214.71624	52.600051	23.54	26.00	1.000	43.00	112±14	-14.1	...	214.71530	52.599945	2.1	0.986 ^b	AGN
GALEX142242+525245	215.67896	52.879323	22.07	-26.74	1.003	42.65	12±3	215.67851	52.879360	1.0	0.999 ^b	...
GALEX142033+530617	215.14121	53.104797	23.62	25.29	0.999	42.80	75±8	-14.5	...	215.14162	53.105114	1.5	0.994 ^b	...
GALEX141902+525637	214.76161	52.943789	22.47	24.55	0.984	42.56	21±4	214.76091	52.943871	1.6	0.980 ^b	...
GALEX142207+525411	215.52938	52.903111	23.07	25.35	0.996	43.16	104±5	215.52910	52.902931	0.9	0.994 ^b	AGN
GALEX142148+522902	215.45007	52.484033	23.04	27.40	0.961	43.23	131±13	215.44913	52.484470	2.6	0.961 ^b	...
GALEX142244+525442	215.68588	52.911824	23.85	26.89	0.958	43.26	300±22	215.68564	52.911930	0.6	0.954 ^b	...
GALEX141746+525259	214.44522	52.882997	24.17	-27.28	0.957	42.58	87±10	214.44400	52.884399	5.7	0.957 ^b	...
GALEX141946+524755	214.94289	52.798752	22.23	28.91	0.928	42.21	6±3	214.94319	52.798855	0.7	0.914 ^b	...
GALEX141935+524127	214.89632	52.690888	22.13	24.21	0.920	42.72	20±3	214.89662	52.690529	1.4	0.917 ^b	...
GALEX141733+530403	214.39094	53.067620	23.21	24.87	0.918	43.07	120±10	214.39050	53.067913	1.4	0.915 ^b	AGN
GALEX141833+525525	214.64107	52.923739	23.46	26.32	0.916	42.74	72±7	214.64212	52.924011	2.5	0.912 ^b	...
GALEX142201+530637	215.50453	53.110604	24.13	25.62	0.912	43.19	398±53	-13.3	...	215.50462	53.110195	1.5	0.898 ^b	AGN
GALEX142202+530823	215.50844	53.139988	22.85	24.75	0.872	215.50819	53.140114	1.3	(0.572) ^b	...
GALEX142028+525839	215.11758	52.977690	23.30	-27.77	0.870	42.81	83±8	-13.9	...	215.11682	52.978155	2.3	0.871 ^c	...
GALEX141800+522514	214.50369	52.420519	22.59	25.99	0.838	42.89	60±5	214.50280	52.419863	3.1	0.833 ^c	...
GALEX141722+524209	214.34177	52.702458	22.26	26.40	0.838	43.07	65±5	214.34238	52.702278	1.5	0.838 ^c	...
GALEX142202+522931	215.50918	52.492172	24.88	28.45	0.812	42.66	307±52	215.51004	52.493038	3.6	0.807 ^b	...
GALEX142223+525642	215.59777	52.945235	23.55	26.86	0.770	42.90	187±21	215.59738	52.944958	1.3	0.763 ^b	...
GALEX141858+523209	214.74578	52.535948	21.76	22.67	0.762	43.11	57±4	-14.4	...	214.74509	52.536110	1.6	0.758 ^b	AGN
GALEX142049+523203	215.20764	52.534438	23.62	28.61	0.754	43.03	273±21	215.20830	52.534378	1.5	0.758 ^b	...
GALEX142212+522634	215.55384	52.443058	23.67	27.45	0.762	42.47	79±11	215.55397	52.443161	0.5	0.759 ^b	...
GALEX142057+525642	215.24117	52.945171	22.54	24.98	0.756	43.00	101±6	215.24106	52.944958	0.8	0.747 ^b	...
GALEX141746+525646	214.44476	52.946049	23.28	25.21	0.750	42.97	191±22	214.44504	52.946918	3.2	0.746 ^b	AGN
GALEX141842+522256	214.67524	52.382180	23.65	26.29	0.750	42.49	85±16	214.67545	52.381447	2.7	0.747 ^b	...
GALEX141842+530140	214.67697	53.027806	23.03	25.01	0.748	42.59	62±9	214.67871	53.028191	4.0	0.741 ^b	...
GALEX142139+523401	215.41400	52.567205	23.82	26.24	0.741	AGN	215.41359	52.568192	3.8	(0.692) ^b	...

Note. —

^a X-ray data from Laird et al. (2009)

^b This paper's DEIMOS spectra

^c Archival DEIMOS DEEP2 spectra (Newman et al. 2012)

^d [alt] Alternative counterpart at 215.05445, 52.667969, 4.4, no z (R.A., Decl., Offset, z_{opt})

Table 6
Emission-line Sample: NGPDWS-00

Name	R.A.	Decl.	NUV	FUV	z_{galax}	$\log L(\text{Ly}\alpha)$	$\text{EW}_{\text{r}}(\text{Ly}\alpha)$	$\log f_{2-7}^{\alpha}$	Type(UV)	R.A.(opt)	Decl.(opt)	Offset	z_{opt}	Type(opt)
(1)	(J2000.0)	(J2000.0)	(AB)	(AB)	(6)	(erg s^{-1})	(\AA)	($\text{erg cm}^{-2}\text{s}^{-1}$)	(10)	(J2000.0)	(J2000.0)	(arcsec)	(14)	(15)
GALEX143557+350702	218.98764	35.117445	23.82	-28.46	1.158	43.27	169±26	218.98735	35.116795	2.5	1.152 ^b	...
GALEX143539+351001	218.91250	35.167233	22.20	25.99	1.083	43.40	63±6	218.91272	35.167511	1.2	1.082 ^b	...
GALEX143545+350039	218.93744	35.011330	24.17	26.63	1.063			...	AGN	218.93967	35.010777	5.9	(0.722) ^b	...
GALEX143520+350414	218.83421	35.070876	21.55	22.69	1.055	43.32	31±3	-14.5	...	218.83405	35.070351	2.0	1.052 ^b	AGN
GALEX143824+352325	219.60174	35.390787	21.92	24.92	1.039	42.92	18±3	...	AGN	219.60257	35.390755	2.4	1.031 ^b	...
GALEX143512+352338	218.80005	35.394162	24.84	-31.03	1.037			218.80109	35.392956	4.2	(1.080) ^{b,c}	...
GALEX143726+351448	219.36103	35.247140	22.44	24.39	1.034	43.13	47±6	-15.1 ^e
GALEX143443+353037	218.68009	35.510756	23.39	28.50	1.034	42.85	61±8	218.68036	35.510929	1.0	1.025 ^b	...
GALEX143750+350645	219.45954	35.112962	22.22	23.70	1.010			-15.0	...	219.46024	35.113098	1.9	(0.577) ^b	...
GALEX143449+350248	218.70428	35.046988	23.21	29.53	1.009	43.60	303±9	-15.3
GALEX143810+350424	219.54441	35.073741	23.73	26.81	1.006	43.15	177±14	219.54455	35.073328	0.7	no z	...
GALEX143450+352520	218.70844	35.422650	22.85	26.74	0.967	43.29	122±7	-14.2	...	218.70876	35.422508	1.1	0.964 ^b	AGN
GALEX143512+345907	218.79986	34.985750	24.58	28.79	0.963			218.80116	34.984894	3.8	(0.884) ^b	...
GALEX143510+351602	218.79406	35.267619	23.42	26.28	0.941			218.79521	35.267330	2.5	(0.478) ^{b,d}	...
GALEX143639+350557	219.16252	35.099672	22.31	23.43	0.937	42.87	32±3	219.16257	35.099346	1.2	0.932 ^b	...
GALEX143702+350155	219.26169	35.032282	22.94	24.99	0.933	43.34	149±10	-14.6	...	219.26167	35.032078	0.7	0.927 ^b	AGN
GALEX143531+351415	218.88092	35.237743	23.09	27.50	0.934	42.96	78±11	218.88094	35.238354	2.2	0.930 ^b	...
GALEX143730+352016	219.37524	35.338103	22.51	24.34	0.907	42.90	46±5	219.37563	35.337757	1.7	0.904 ^b	AGN
GALEX143521+350509	218.83940	35.086214	21.89	26.57	0.901			218.83961	35.085414	2.1	star	star
GALEX143819+351542	219.58154	35.262070	23.01	26.70	0.889	42.63	39±9	219.58224	35.261349	3.3	0.889 ^b	...
GALEX143652+350537	219.21699	35.093944	21.90	23.03	0.870	43.25	63±5	-15.0	...	219.21677	35.093887	0.7	0.866 ^b	AGN
GALEX143729+350732	219.37419	35.125830	22.68	24.16	0.868	43.31	151±11	-15.0	...	219.37398	35.126053	1.0	0.860 ^b	AGN
GALEX143457+353213	218.73762	35.537287	21.75	23.02	0.865	42.82	21±3	-14.9	...	218.73782	35.537319	0.6	0.857 ^b	AGN
GALEX143715+353355	219.31319	35.565674	22.38	23.84	0.854	43.27	127±11	-15.1 ^e	...	219.31288	35.565460	1.2	0.846 ^b	AGN
GALEX143459+352504	218.74643	35.418085	22.48	-28.10	0.848			218.74582	35.417044	4.0	star	star
GALEX143800+352206	219.50182	35.368824	22.24	24.81	0.829	42.81	35±5	-15.4
GALEX143642+345027	219.17868	34.841281	24.09	27.73	0.823	42.91	254±49	219.17896	34.841167	0.9	0.818 ^b	...
GALEX143655+344610	219.23087	34.769857	24.20	28.61	0.820	42.88	269±30	219.23146	34.769501	2.2	0.813 ^b	...
GALEX143801+352533	219.50452	35.426310	21.62	22.75	0.806	43.09	42±3	-14.7
GALEX143700+353132	219.25323	35.525830	22.50	24.40	0.791	42.96	75±7	219.25333	35.525555	1.0	0.784 ^b	AGN
GALEX143515+353203	218.81441	35.534506	21.77	23.47	0.789			218.81459	35.534233	0.5	(0.410) ^b	...
GALEX143821+350707	219.59055	35.118996	21.62	23.15	0.741	43.23	75±5	-14.8	AGN	219.59068	35.119396	1.5	0.728 ^b	...
GALEX143829+352308	219.62144	35.385905	22.19	24.26	0.720	42.49	25±4	219.62173	35.385715	1.1	0.710 ^b	...
GALEX143716+352324	219.32011	35.390438	24.61	27.67	0.716	42.61	365±65	219.31993	35.391083	2.4	0.699 ^b	...
GALEX143813+351121	219.55694	35.189666	24.20	27.14	0.710	42.67	199±53	219.55760	35.190166	2.6	0.717 ^b	...

Note. —

^a X-ray data from Kenter et al. (2005)

^b This paper's DEIMOS spectra

^c [alt] Alternative counterpart at 218.98737, 35.115852, 5.8, (1.096)^b (R.A., Decl., Offset, z_{opt})

^d [alt] Alternative counterpart at 218.79877, 35.394573, 4.0, (0.977)^b (R.A., Decl., Offset, z_{opt})

^e Source not detected in X-ray hard band but detected in the soft 0.5-2 keV flux band

Table 7
Emission-line Sample: COSMOS-00

Name	R.A.	Decl.	NUV	FUV	z_{galax}	$\log L(\text{Ly}\alpha)$	$\text{EW}_r(\text{Ly}\alpha)$	$\log f_{2-10}^a$	Type(UV)	R.A.(opt)	Decl.(opt)	Offset	z_{opt}	Type(opt)
(1)	(J2000.0)	(J2000.0)	(AB)	(AB)	(6)	(erg s^{-1})	(\AA)	($\text{erg cm}^{-2}\text{s}^{-1}$)	(10)	(J2000.0)	(J2000.0)	(arcsec)	(14)	(15)
GALEX095954+021707	149.97779	2.2852787	22.17	23.93	1.163	43.24	30±4	-14.7
GALEX100145+023237	150.43904	2.5436927	23.59	24.84	1.154	43.35	158±13	150.43942	2.5435109	1.5	1.149 ^b	AGN
GALEX100016+015104	150.06776	1.8512265	21.74	23.40	1.140	43.63	57±4	-13.6	AGN	150.06784	1.8513390	0.5	1.134 ^b	AGN
GALEX100031+023012	150.13260	2.5034525	22.72	25.38	1.103	43.21	59±6	150.13235	2.5033109	1.0	1.099 ^{b,c}	...
GALEX095918+014933	149.82753	1.8260336	22.89	25.11	1.070	43.38	109±10	149.82774	1.8258640	1.0	1.069 ^{b,c}	...
GALEX095916+015048	149.81704	1.8467845	21.94	24.30	1.034	43.20	33±4	-14.0	AGN	149.81688	1.8467280	0.6	1.034 ^b	AGN
GALEX100141+021029	150.42197	2.1748164	21.83	23.00	0.989	43.47	65±5	-13.5	AGN	150.42221	2.1754150	2.3	0.982 ^d	AGN
GALEX100150+020936	150.45907	2.1598448	22.75	25.61	0.927	43.11	79±7	150.45946	2.1603360	2.3	0.926 ^{b,c}	AGN
GALEX100124+021447	150.34970	2.2463910	22.34	23.46	0.900	43.23	77±8	-13.8	...	150.34988	2.2461319	1.1	0.894 ^d	...
GALEX100202+020145	150.51078	2.0290676	22.95	24.72	0.894	43.20	124±9	-13.6	...	150.51064	2.0292540	0.8	0.898 ^d	AGN
GALEX100049+021707	150.20630	2.2852412	23.88	24.96	0.877	42.96	181±30	-13.7	...	150.20627	2.2857921	2.0	0.874 ^d	AGN
GALEX100136+020653	150.40266	2.1148013	22.28	25.06	0.853	42.92	42±5	150.40346	2.1155031	3.8	0.849 ^{b,c}	...
GALEX100133+015451	150.39033	1.9141639	21.85	24.96	0.848	43.02	37±3	150.39020	1.9144530	1.1	0.844 ^{b,c}	...
GALEX100002+021628	150.00988	2.2746592	21.90	23.78	0.847	42.99	34±4	-13.5	...	150.00922	2.2755051	3.9	0.850 ^d	AGN
GALEX100207+021119	150.53190	2.1886307	22.31	22.60	0.838	43.25	101±19	-14.0	...	150.53186	2.1889460	1.1	0.830 ^d	...
GALEX100113+022548	150.30739	2.4301342	22.76	23.40	0.757			-13.6	...	150.30808	2.4300640	2.5	(0.374) ^e	AGN
GALEX100029+022129	150.12442	2.3581919	22.26	23.42	0.739	42.93	66±9	-13.6	AGN	150.12370	2.3582580	2.6	0.728 ^e	AGN
GALEX095910+020732	149.79323	2.1258027	22.12	22.22	0.730			-14.8 ^f	...	149.79295	2.1256490	1.1	(0.353) ^d	...
GALEX100017+020013	150.07274	2.0037061	22.69	23.04	0.729			-13.6	...	150.07301	2.0035551	1.1	(0.350) ^d	AGN

Note. —

^a X-ray data from Elvis et al. (2009)

^b This paper's DEIMOS spectra

^c This paper's SALT spectra

^d Archival Magellan spectra from Trump et al. (2009)

^e Archival VLT spectra from Lilly et al. (2007)

^f Source not detected in X-ray hard band but detected in the soft 0.5-2 keV flux band